

**PERFORMANCE ANALYSIS OF POINT SOURCE MODEL WITH
COINCIDENT PHASE CENTERS IN FDTD**

by

Yang Xu

A Thesis

Submitted to the Faculty

of the

WORCESTER POLYTECHNIC INSTITUTE

in partial fulfillment of the requirements for the

Degree of Master of Science

in

Electrical and Computer Engineering

March 2014

APPROVED:

Dr. Sergey N Makarov, Major Advisor

Dr. Vishwanath Iyer

Gregory M. Noetscher

ABSTRACT

The Finite Difference Time Domain (FDTD) Method has been a powerful tool in numerical simulation of electromagnetic (EM) problems for decades. In recent years, it has also been applied to biomedical research to investigate the interaction between EM waves and biological tissues. In Wireless Body Area Networks (WBANs) studies, to better understand the localization problem within the body, an accurate source/receiver model must be investigated. However, the traditional source models in FDTD involve effective volume and may cause error in near field arbitrary direction.

This thesis reviews the basic mathematical and numerical foundation of the Finite Difference Time Domain method and the material properties needed when modeling a human body in FDTD. Then Coincident Phase Centers (CPCs) point sources models have been introduced which provide nearly the same accuracy at the distances as small as 3 unit cells from the phase center. Simultaneously, this model outperforms the usual sources in the near field when an arbitrary direction of the electric or magnetic dipole moment is required.

Keywords: Finite Difference Time Domain Method, Infinitesimal Electric Dipole, Infinitesimal Magnetic Dipole, Point Source, Source Modeling, Wireless Body Area Networks, Localization

ACKNOWLEDGEMENTS

With a deep sense of gratitude, I wish to express my sincere thanks to my advisor, Professor Sergey N. Makarov, for his encouragement, suggestions, and great help in the past years. His profound knowledge, professional working attitude and Shining personality have a significant influence in my future life.

I would also like to thank my committee members, Mr. Gregory Noetscher and Dr. Vishwanath Iyer, for their valuable advises and carefully reviewing my thesis.

Personally I would like to give special thank to my parents, Dongfang Xu and Hongxia Fang, for your endless love and fostering my curiosity from childhood. It has been a tough time for our family during the past 2 years, without your support I cannot made it this far.

Finally, my heartfelt appreciation goes to my girlfriend who has never appeared in the past 26 years, which enables me to focus on my research and study. Thank you so much.

Table of Contents

ABSTRACT	I
ACKNOWLEDGEMENTS.....	II
Table of Contents	III
List of Figures.....	V
List of Tables.....	VI
CHAPTER 1 INTRODUCTION	1
1.1 Research Background.....	1
1.2 Thesis Overview	1
CHAPTER 2 FINITE DIFFERENCE TIME DOMAIN METHOD	3
2.1 Maxwell's equations.....	3
2.1.1 Lossless space with no sources	3
2.1.2 Driving sources and lossy space	4
2.2 The Yee algorithm	5
2.2.1 Half-grid formulation.....	7
2.2.2 Numerical (integer spatial indexes) formulation.....	9
2.2.3 Exponential time stepping.....	11
2.3 Materials properties in FDTD	12
2.4 Absorbing Boundary Conditions	13
2.4.1 Mur's ABCs	14
2.4.2 Implementation of the first-order Mur's ABCs.....	16
2.4.3. "Superabsorption" ABCs	17
2.5 Perfectly Matched Layer (PML)	19
CHAPTER 3 COINCIDENT PHASE CENTER ANTENNA	26
3.1 Electric dipole model.....	26
3.1.1 Standard small dipole model.....	26
3.1.2 Coincident Phase Centers dipole model for arbitrary orientation	27
3.2 Magnetic dipole (coil antenna) model	29
3.2.1 General facts about coil antennas.....	29
3.2.2 Receive Coil	31
3.2.2.1 Coil without magnetic core	31
3.2.2.2 Coil with arbitrary orientation.....	32
3.2.2.3. Coil with a magnetic core.....	32
3.2.3 Transmit coil - a magnetic dipole	32
3.2.3.1 Magnetic dipole	32
3.2.3.2 Magnetic dipole model with a magnetic current source	33
3.2.3.3 Magnetic dipole model with a loop of electric current.....	34
3.2.3.4 Magnetic dipole model with Coincident Phase Centers for arbitrary coil orientation.....	36
3.2.4. Mutual inductance between transmit and receive coils	39
3.3 Model of an impressed electric field or voltage source (loop of magnetic current).....	39
3.3.1. Concept of an impressed voltage (electric field) source	39
3.3.2. Modeling an impressed voltage source	40

3.3.3. Modeling an impressed voltage source with Coincident Phase Centers.....	42
3.3.4. Relation between the magnetic current loop source and the electric dipole source.....	43
3.4 Performance validation	45
3.4.1 Pulse form to be used	45
3.4.2 Transmit (TX) Electrical dipole case	46
3.4.3 Arbitrarily oriented Electric TX dipole(s)	48
3.4.4 TX coil in free space.....	51
3.4.5 TX and RX coils in free space.....	54
3.4.6 Arbitrarily oriented TX and RX coils in free space	57
3.4.7 Impressed voltage (electric-field) source in free space.....	60
3.4.8 Error Analysis.....	63
3.4.9 Analysis of the closest distance.....	64
CHAPTER 4 CONCLUSIONS.....	66
BIBLIOGRAPHY.....	67

List of Figures

Figure 2-1 Yee unit cell	7
Figure 2-2 A numbering scheme suitable for programming	9
Figure 2-3 Standard field nodes and material parameter nodes. The permittivity/conductivity is defined at cell centers. The permeability/magnetic loss is defined at cell corners	13
Figure 2-4 An "almost" plane wave that is coming toward the boundaries needs to be absorbed ...	14
Figure 2-5 Superabsorption ABCs on the right boundary	18
Figure 2-6 The PML concept for the TE to z field	20
Figure 2-7 The PML concept for the TM to z field	21
Figure 2-8 different conductivity in different PML regions.....	22
Figure 2-9 A sketch of one 2D PML grid with sides and corners	24
Figure 2-10 3D PML regions – 6 Sides, 12 Edges and 8 Corners	25
Figure 3-1 Dipole antenna with the impressed line current $i_s(t)$	26
Figure 3-2 Dipole antenna model with the dipole placed at the center node of the Yee cell.....	27
Figure 3-3 A coil antenna (with or without) the magnetic core.....	30
Figure 3-4 Coil antenna modeled with a loop of an equivalent electric current.....	34
Figure 3-5 Coil antenna model with the coil placed at the center node of the Yee cell	36
Figure 3-6 Impressed voltage (electric field source).....	40
Figure 3-7 TX voltage source and the surrounding FDTD grid	41
Figure 3-8 Impressed source model with the dipole placed at the corner node of the Yee cell.....	43
Figure 3-9 a) Test geometry and b) Test output.....	46
Figure 3-10 Comparison results for a)20mm and b)10mm cell size. Blue – exact analytical solution; red – FDTD.	48
Figure 3-11 a) Test geometry and b) Test output	49
Figure 3-12 Comparison results for a) 20mm and b) 10mm cell size. Blue – exact analytical solution; red – FDTD.	51
Figure 3-13 a)Test geometry and b) Test output.....	52
Figure 3-14 Comparison results for a) 20mm and b) 10mm cell size. Blue – exact analytical solution; red – FDTD.	54
Figure 3-15 a)Test geometry and b) Test output.....	55
Figure 3-16 Comparison results for a) 20mm and b) 10mm cell size. Blue – exact analytical solution; red – FDTD.	57
Figure 3-17 a)Test geometry and b) Test output.....	58
Figure 3-18 Comparison results for a) 20mm and b) 10mm cell size. Blue – exact analytical solution; red – FDTD.	60
Figure 3-19 a)Test geometry and b) Test output.....	61
Figure 3-20 Comparison results for a) 20mm and b) 10mm cell size. Blue – exact analytical solution; red – FDTD.	63
Figure 3-21 Copolar fields close to the dipole (top) and coil (bottom) as spacing moves from one cell (left) to three (right).....	65
Figure 4-1 Geometry and H-plane definition (left) and normalized patterns into the lower half-space (right).....	66

List of Tables

Table 3-1 CARTESIAN CURRENT DENSITY COMPONENTS	45
Table 3-2 Test parameters	46
Table 3-3 Test parameters	49
Table 3-4 Test parameters	52
Table 3-5 Test parameters	54
Table 3-6 Test parameters	57
Table 3-7 Test parameters	60
Table 3-8 RELATIVE ERRORS COMPARISON BETWEEN STANDARD MODEL AND CPCs MODEL	64
Table 3-9 EXAMINATION OF SOURCE SEPARATION	65

CHAPTER 1

INTRODUCTION

1.1 Research Background

Since the introduction of the Finite-Difference Time-Domain (FDTD) method by K. S. Yee in 1966 [1], it has been widely applied in many critical areas such like simulating complicated physical phenomena and improving innovation in key electrical engineering areas ranging from radar system to consumer electronics and cellphones [2]. Given its nature simplicity — without having to derive Green's Functions or to solve system of matrix equations — and its good scalability when handling complex inhomogeneous/dispersive media problems, FDTD has become very popular in recent emerging cross-discipline areas like Wireless Body Area Networks (WBANs) field [3]. In WBANs, a crucial problem is how to model electrically small antennas and sensors, both in free space and in the presence of electrically lossy media. WBANs may run around 400MHz which result in a wavelength of ~ 1 meter. To accurately model antennas and sensors around or inside human body which is characterized by wavelengths usually less than 10 centimeters, very fine meshes should be used. The treatment of the radiation source within the FDTD method is fundamental to this problem and the topic of this thesis.

In the past decades continuous research has been pursued in an effort to expand the applications of the method while reducing errors and uncertainties inherent in digitally implemented simulations. While true continuous-time analogue operation from a digital computer is theoretically unattainable in practice, it is with the goal of ever improving performance in mind that enhancements in modeling and simulation techniques are proposed and tested. In this way, accurate and timely engineering tools can be created that address these complex electromagnetic applications in WBANs.

In the limit, an infinitesimal radiator, whether electrical or magnetic in nature, approaches an electric or magnetic dipole moment. While infinitesimally small dipoles are usually of little practical value, they represent the building blocks for more intricate geometries and proper understanding of these components can facilitate more accurate antenna modeling.

1.2 Thesis Overview

Traditional modeling of small electric (magnetic) dipoles involves the creation of an asymmetric point source oriented along a cell edge (face center) consistent with the electric (magnetic) field node that serves as the field supply. As described below, this methodology allows for the smallest possible size of one cell (as constrained by the structured FDTD mesh) but distributes the source in such a way that the phases of the

three cartesian source components are slightly different from each other. While this inconsistency is acceptable for many modeling problems, phase inaccuracies can be extremely detrimental when simulating highly phase sensitive including signal Time of Arrival (ToA) and Direction of Arrival (DoA) estimation, which, among other things, use phase data for high precision ultrawideband (UWB) geo-location [3] and antenna array beamforming [4], respectively.

This thesis introduces a new, arbitrarily oriented symmetric point source model with coincident phase centers (CPCs) for electric and magnetic dipoles, electric field sources and probe modeling. The analytical and numerical results will show that, despite the larger averaging volume, the point sources with CPCs provide accuracies that are very comparable to standard sources with observation distances as small as 3 unit cells from the phase center. Simultaneously, these sources outperform standard sources in the near field when an arbitrary direction of the electric or magnetic dipole moment is required.

Chapter II gives the basic mathematical foundation of Maxwell's equations in electromagnetics problems and the fundamental idea of FDTD method, as well as the Yee discretization method of space grids. Since the original Yee grid is not convenient in practical implementation, an alternative integer-based scheme has been introduced to solve the issue. A unified materials property modeling method is described in this chapter as well. At the very end of this chapter, Absorbing Boundary Conditions (ABCs) are discussed. There are varieties of ABCs that have been investigated in the past decades including Mur's ABCs and the so called Perfectly Matched Layer (PML),etc. Here, Mur's first and second order ABCs with a superabsorption enhancement have been adopted because of its balance in simplicity and performance.

Chapter III gives the theoretical model and implementation details of both standard and CPCs point source in different scenarios including electric dipole, magnetic dipole (coil) and impressed voltage source. By comparing with the analytical solution, a number of test cases have been conducted as benchmarks: 1) Transmit electric dipole, 2) Arbitrarily oriented electrical dipole, 3) Transmit magnetic dipole (coil), 4) Transmit and receive coils, 5) Arbitrarily oriented coil, 6) Impressed voltage source. Performance validation indicates that the CPCs model can well describe the arbitrarily oriented cases and remains a good approximation to grid-aligned cases. Finally, an analysis of the closest distance between the transmit and receive antennas has been performed. It is proved that at a spacing of three grid cells, a very good match can be achieved and even with a spacing of one cell, the magnetic dipole (coil) still gives a reasonable performance.

Chapter IV concludes this thesis and lists some future possible research directions.

CHAPTER 2

FINITE DIFFERENCE TIME DOMAIN METHOD

2.1 Maxwell's equations

From a long view of the history of mankind - seen from, say, ten thousand years from now - there can be little doubt that the most significant event of the 19th century will be judged as Maxwell's discovery of the laws of electrodynamics — Richard P Feynman.

In 1861, by introducing the displacement current term in Ampere's law, Scottish mathematician and physicist James Clerk Maxwell concluded the achievements from previous scientists Charles-Augustin de Coulomb, André-Marie Ampère, and Michael Faraday, etc., and developed a series of equations to describe universal electromagnetic phenomena, and predict light propagating as electromagnetic waves. It has driven most technology progress in the past centuries and become the foundation of modern electrical engineering.

2.1.1 Lossless space with no sources

For simplicity, a propagation problem in lossless freespace is given as the beginning.

Consider an arbitrary (inhomogeneous) medium with electric permittivity ε having the units of F/m and with magnetic permeability μ having the units of H/m. In free lossless space (space without sources), Maxwell's equations for the electric field (or the electric field intensity) \vec{E} [V/m] and for the magnetic field (or the magnetic field intensity) \vec{H} [A/m] in time domain have the form

$$\text{Maxwell's } \nabla \times \vec{H} \text{ equation} \quad \varepsilon \frac{\partial \vec{E}}{\partial t} = \nabla \times \vec{H} \quad (2-1a)$$

$$\text{Faraday's law} \quad \mu \frac{\partial \vec{H}}{\partial t} = -\nabla \times \vec{E} \quad (2-1b)$$

$$\text{Gauss' law for electric field (no electric charges)} \quad \nabla \cdot \varepsilon \vec{E} = 0 \quad (2-1c)$$

$$\text{Gauss' law for magnetic field (no magnetic charges)} \quad \nabla \cdot \mu \vec{H} = 0 \quad (2-1d)$$

2.1.2 Driving sources and lossy space

By introducing the driving source and lossy in space, the complete Maxwell's equations can be formulated. The driving sources for the electromagnetic fields are given by (generally volumetric) electric current density \vec{J}_s of free charges with the units of A/m², and by volumetric free charge density ρ_s with the units of C/m³. The free charges are free electrons in a metal or free electrons and/or holes in a semiconductor. Instead of volumetric currents one may consider surface currents (for example, on the blade of a metal dipole) or line current (an infinitesimally thin cylindrical dipole/wire).

The driving sources may be also given by a (volumetric) magnetic current density \vec{J}_{ms} with the units of V/m² and by volumetric magnetic charge density ρ_{ms} . The magnetic current density may be associated with an external impressed voltage. However, no magnetic charge has been found to exist in nature. Still, in practice it is often convenient to use the concept of magnetic currents (and fictitious magnetic charges).

The electric conduction current is always present in a lossy medium in the form $\vec{J} = \sigma \vec{E}$ where σ is the electric conductivity with the units of S/m. An analogous magnetic conduction current may be defined describing the magnetic loss mechanism, $\vec{J}_m = \bar{\rho} \vec{H}$ where $\bar{\rho}$ is the magnetic resistivity with the units of Ω/m .

In a lossy space with driving sources, Maxwell's equations for the electric field (or the electric field intensity) \vec{E} [V/m] and for the magnetic field (or the magnetic field intensity) \vec{H} [A/m] in time domain have the form

Ampere's law modified by displacement currents
$$\epsilon \frac{\partial \vec{E}}{\partial t} = \nabla \times \vec{H} - \vec{J} - \vec{J}_s \quad (2-2a)$$

Faraday's law
$$\mu \frac{\partial \vec{H}}{\partial t} = -\nabla \times \vec{E} - \vec{J}_m - \vec{J}_{ms} \quad (2-2b)$$

Gauss' law for electric field
$$\nabla \cdot \epsilon \vec{E} = \rho_s \quad (2-2c)$$

Gauss' law for magnetic field (no magnetic charges) $\nabla \cdot \mu \vec{H} = \rho_{ms}$ (2-2d)

The continuity equation for the impressed electric current can be derived from these

equations above: $\frac{\partial \rho_s}{\partial t} + \nabla \cdot \vec{J}_s = 0$ (2-2e)

The analytical solution of Maxwell's equations has been studied for years, with much progress achieved. However, in many complex real engineering applications which include non-uniform boundary conditions and complicated geometric structures, the analytical solution is too complicated to be tractable. At this time numerical method becomes an alternative and powerful tool to handle these problems with arbitrary geometries and boundary conditions. FDTD is one such method and has been widely used in recent years.

2.2 The Yee algorithm

The basic idea of the FDTD method is based on the traditional finite difference method to solve partial differential equations numerically. The differential may be approximated as

$$\left. \frac{df(x)}{dx} \right|_{x=x_0} = \frac{f(x_0 + \Delta x/2) - f(x_0 - \Delta x/2)}{\Delta x} \quad (2-3)$$

with second order accuracy, which can be derived from Taylor series:

$$f(x_0 + \frac{\Delta x}{2}) = f(x_0) + \frac{\Delta x}{2} f'(x_0) + \frac{1}{2!} \left(\frac{\Delta x}{2} \right)^2 f''(x_0) + \frac{1}{3!} \left(\frac{\Delta x}{2} \right)^3 f'''(x_0) + \dots \quad (2-4a)$$

$$f(x_0 - \frac{\Delta x}{2}) = f(x_0) - \frac{\Delta x}{2} f'(x_0) + \frac{1}{2!} \left(\frac{\Delta x}{2} \right)^2 f''(x_0) - \frac{1}{3!} \left(\frac{\Delta x}{2} \right)^3 f'''(x_0) + \dots \quad (2-4b)$$

By adding them together,

$$f(x_0 + \frac{\Delta x}{2}) - f(x_0 - \frac{\Delta x}{2}) = \Delta x f'(x_0) + \frac{2}{3!} \left(\frac{\Delta x}{2} \right)^3 f'''(x_0) + \dots \quad (2-5)$$

Divide by Δx We can get

$$\frac{f(x_0 + \frac{\Delta x}{2}) - f(x_0 - \frac{\Delta x}{2})}{\Delta x} = f'(x_0) + \frac{1}{3!} \frac{\Delta x^2}{2^2} f'''(x_0) + \dots$$

(2-6)

This may be rewritten as

$$\begin{aligned} f'(x_0) &= \left. \frac{df(x)}{dx} \right|_{x=x_0} = \frac{f(x_0 + \frac{\Delta x}{2}) - f(x_0 - \frac{\Delta x}{2})}{\Delta x} - \frac{1}{3!} \frac{\Delta x^2}{2^2} f'''(x_0) + \dots \\ &= \frac{f(x_0 + \frac{\Delta x}{2}) - f(x_0 - \frac{\Delta x}{2})}{\Delta x} + O(\Delta x^2) \end{aligned}$$

(2-7)

The $O(\Delta x^2)$ term indicates a second order accuracy here.

While it is simple in the one-dimension case, to develop a stable 3-D framework for general electromagnetics problem discretization was not accomplished until 1966, when K. S. Yee published a paper proposing an elegant discretization scheme to solve this problem.

A cubic Yee unit cell (uniform cell size Δ in all directions) is shown in Fig. 2-1. It has the following features [1]:

1. The electric field is defined at the edge centers of a cube;
2. The magnetic field is defined at the face centers of a cube;
3. The electric permittivity/conductivity is defined at the cube center(s);
4. The magnetic permeability/magnetic loss is defined at the cube nodes (corners).

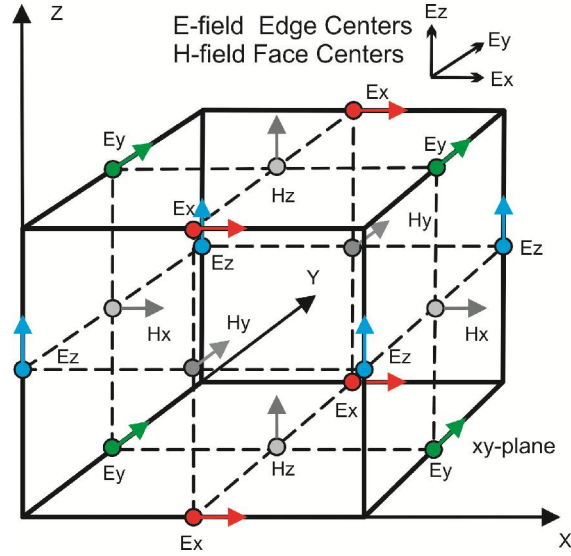


Figure 2-1 Yee unit cell

Therefore, four interleaving indexing systems (i,j,k) in space may be introduced and used simultaneously:

1. the system based on cube edge centers (for the electric field);
2. the system based on cube face centers (for the magnetic field);
3. the system based on cube centers (for electric permittivity/conductivity values);
4. the system based on cube nodes (for magnetic permeability/magnetic loss values);

The interleaving feature of those systems is mathematically described by half-integer indexes. For example, when the indexing system for the magnetic field is used, the nodal magnetic field $H_y|_{i,j,k}$ is located exactly halfway between electric field nodes

$E_z|_{i-1/2,j,k}$ and $E_z|_{i+1/2,j,k}$ in Fig. 2-1. Similarly, when the indexing system for the

electric field is used, the nodal electric field $E_z|_{i,j,k}$ is located exactly halfway

between magnetic field nodes $H_y|_{i-1/2,j,k}$ and $H_y|_{i+1/2,j,k}$ in Fig. 2-1, except for the

boundary nodes.

2.2.1 Half-grid formulation

Applying the central differences to all derivatives in Eqs. (2-1) and denoting the temporal grid by a superscript n , one arrives at the following finite-difference update

equations [2]:

Determine magnetic field at half temporal grid using the past values of the magnetic and electric fields:

$$H_x|_{i,j,k}^{n+1/2} = H_{x1}|_{i,j,k} H_x|_{i,j,k}^{n-1/2} + H_{x2}|_{i,j,k} \left(E_y|_{i,j,k+1/2}^n - E_y|_{i,j,k-1/2}^n + E_z|_{i,j-1/2,k}^n - E_z|_{i,j+1/2,k}^n \right) \quad (2-8a)$$

$$H_y|_{i,j,k}^{n+1/2} = H_{y1}|_{i,j,k} H_y|_{i,j,k}^{n-1/2} + H_{y2}|_{i,j,k} \left(E_z|_{i+1/2,j,k}^n - E_z|_{i-1/2,j,k}^n + E_x|_{i,j,k-1/2}^n - E_x|_{i,j,k+1/2}^n \right) \quad (2-8b)$$

$$H_z|_{i,j,k}^{n+1/2} = H_{z1}|_{i,j,k} H_z|_{i,j,k}^{n-1/2} + H_{z2}|_{i,j,k} \left(E_x|_{i,j+1/2,k}^n - E_x|_{i,j-1/2,k}^n + E_y|_{i-1/2,j,k}^n - E_y|_{i+1/2,j,k}^n \right) \quad (2-8c)$$

Determine electric field at integer temporal grid using the past values of the magnetic and electric fields:

$$E_x|_{i,j,k}^{n+1} = E_{x1}|_{i,j,k} E_x|_{i,j,k}^n + E_{x2}|_{i,j,k} \left(H_z|_{i,j+1/2,k}^{n+1/2} - H_z|_{i,j-1/2,k}^{n+1/2} + H_y|_{i,j,k-1/2}^{n+1/2} - H_y|_{i,j,k+1/2}^{n+1/2} \right) \quad (2-8d)$$

$$E_y|_{i,j,k}^{n+1} = E_{y1}|_{i,j,k} E_y|_{i,j,k}^n + E_{y2}|_{i,j,k} \left(H_x|_{i,j,k+1/2}^{n+1/2} - H_x|_{i,j,k-1/2}^{n+1/2} + H_z|_{i-1/2,j,k}^{n+1/2} - H_z|_{i+1/2,j,k}^{n+1/2} \right) \quad (2-8e)$$

$$E_z|_{i,j,k}^{n+1} = E_{z1}|_{i,j,k} E_z|_{i,j,k}^n + E_{z2}|_{i,j,k} \left(H_y|_{i+1/2,j,k}^{n+1/2} - H_y|_{i-1/2,j,k}^{n+1/2} + H_x|_{i,j-1/2,k}^{n+1/2} - H_x|_{i,j+1/2,k}^{n+1/2} \right) \quad (2-8f)$$

The sources may then be added as described by Eqs. (2-2). The electric-field updating coefficients are defined by material properties in the form

$$E_{x1}|_{i,j,k} = \frac{1 - \sigma_{i,j,k} \Delta t / (2\epsilon_{i,j,k})}{1 + \sigma_{i,j,k} \Delta t / (2\epsilon_{i,j,k})}, \quad E_{x2}|_{i,j,k} = \frac{\Delta t / (\epsilon_{i,j,k} \Delta)}{1 + \sigma_{i,j,k} \Delta t / (2\epsilon_{i,j,k})} \quad (2-8g)$$

The same equation applies to E_{y1}, E_{y2} and to E_{z1}, E_{z2} , respectively, but the material properties at the observation node i,j,k may be different.

The magnetic-field updating coefficients are defined by material properties in the

similar form

$$H_{x1}|_{i,j,k} = \frac{1 - \bar{\rho}_{i,j,k} \Delta t / (2\mu_{i,j,k})}{1 + \bar{\rho}_{i,j,k} \Delta t / (2\mu_{i,j,k})}, \quad H_{x2}|_{i,j,k} = \frac{\Delta t / (\mu_{i,j,k} \Delta)}{1 + \bar{\rho}_{i,j,k} \Delta t / (2\mu_{i,j,k})} \quad (2-8h)$$

The same equation applies to H_{y1}, H_{y2} and to H_{z1}, H_{z2} , but the material properties at the observation node i,j,k may be different.

2.2.2 Numerical (integer spatial indexes) formulation

Given that the half-grid representation is quite difficult to program, it will be much more convenient to transfer half integer indices to a global integer index. The corresponding numbering scheme is shown in Fig. 2-2. Here, $G_{i,j,k}$ denotes the reference cube node.

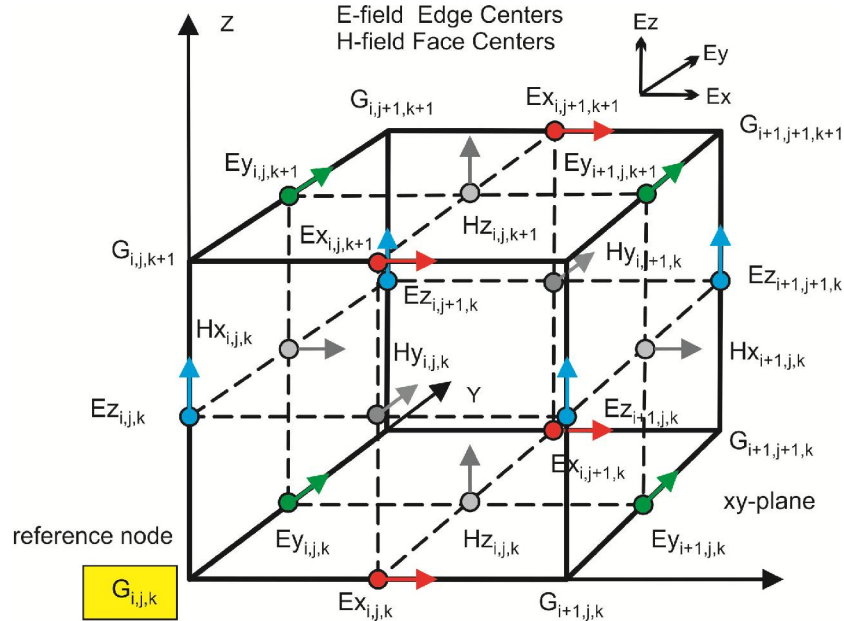


Figure 2-2 A numbering scheme suitable for programming

Eqs. (2-8) may be rewritten in terms of integer indexes. In short, $\pm 1/2$ is replaced by 1 or 0 in the magnetic field update equations, and $\pm 1/2$ is replaced by 0 or -1 in the electric field update equations, respectively. With reference to Fig. 2-2 one has

$$H_x|_{i,j,k}^{n+1/2} = H_{x1}|_{i,j,k} H_x|_{i,j,k}^{n-1/2} + H_{x2}|_{i,j,k} \left(E_y|_{i,j,k+1}^n - E_y|_{i,j,k}^n + E_z|_{i,j,k}^n - E_z|_{i,j+1,k}^n \right) \quad (2-9a)$$

$$H_y|_{i,j,k}^{n+1/2} = H_{y1}|_{i,j,k} H_y|_{i,j,k}^{n-1/2} + H_{y2}|_{i,j,k} \left(E_z|_{i+1,j,k}^n - E_z|_{i,j,k}^n + E_x|_{i,j,k}^n - E_x|_{i,j,k+1}^n \right) \quad (2-9b)$$

$$H_z|_{i,j,k}^{n+1/2} = H_{z1}|_{i,j,k} H_z|_{i,j,k}^{n-1/2} + H_{z2}|_{i,j,k} \left(E_x|_{i,j+1,k}^n - E_x|_{i,j,k}^n + E_y|_{i,j,k}^n - E_y|_{i+1,j,k}^n \right) \quad (2-9c)$$

Determine electric field at integer temporal grid using the past values of the magnetic and electric fields:

$$E_x|_{i,j,k}^{n+1} = E_{x1}|_{i,j,k} E_x|_{i,j,k}^n + E_{x2}|_{i,j,k} \left(H_z|_{i,j,k}^{n+1/2} - H_z|_{i,j-1,k}^{n+1/2} + H_y|_{i,j,k-1}^{n+1/2} - H_y|_{i,j,k}^{n+1/2} \right) \quad (2-9d)$$

$$E_y|_{i,j,k}^{n+1} = E_{y1}|_{i,j,k} E_y|_{i,j,k}^n + E_{y2}|_{i,j,k} \left(H_x|_{i,j,k}^{n+1/2} - H_x|_{i,j,k-1}^{n+1/2} + H_z|_{i-1,j,k}^{n+1/2} - H_z|_{i,j,k}^{n+1/2} \right) \quad (2-9e)$$

$$E_z|_{i,j,k}^{n+1} = E_{z1}|_{i,j,k} E_z|_{i,j,k}^n + E_{z2}|_{i,j,k} \left(H_y|_{i,j,k}^{n+1/2} - H_y|_{i-1,j,k}^{n+1/2} + H_x|_{i,j-1,k}^{n+1/2} - H_x|_{i,j,k}^{n+1/2} \right) \quad (2-9f)$$

To Improve the efficiency when implemented in MATLAB, a vector form is applied as follow.

```

%% H-field update
HxN = Hx1.*HxP + Hx2.*(diff(EyN,1,3) - diff(EzN,1,2));
HyN = Hy1.*HyP + Hy2.*(diff(EzN,1,1) - diff(ExN,1,3));
HzN = Hz1.*HzP + Hz2.*(diff(ExN,1,2) - diff(EyN,1,1));

%% E-field update
ExN(:,2:Ny,2:Nz) =
Ex1.*ExP(:,2:Ny,2:Nz) + Ex2.*(diff(HzP(:, :, 2:Nz), 1, 2) - diff(HyP(:, 2:Ny, :), 1, 3));

EyN(2:Nx, :, 2:Nz) =
Ey1.*EyP(2:Nx, :, 2:Nz) + Ey2.*(diff(HxP(2:Nx, :, :), 1, 3) - diff(HzP(:, :, 2:Nz), 1, 1));

EzN(2:Nx, 2:Ny, :) =
Ez1.*EzP(2:Nx, 2:Ny, :) + Ez2.*(diff(HyP(:, 2:Ny, :), 1, 1) - diff(HxP(2:Nx, :, :), 1, 2));

```

The electric-field updating coefficients are defined by material properties in the same form as before

$$E_{x1}|_{i,j,k} = \frac{1 - \sigma_{i,j,k} \Delta t / (2\epsilon_{i,j,k})}{1 + \sigma_{i,j,k} \Delta t / (2\epsilon_{i,j,k})}, \quad E_{x2}|_{i,j,k} = \frac{\Delta t / (\epsilon_{i,j,k} \Delta)}{1 + \sigma_{i,j,k} \Delta t / (2\epsilon_{i,j,k})} \quad (2-9g)$$

The same equation applies to E_{y1}, E_{y2} and to E_{z1}, E_{z2} , respectively, but the

material properties at the observation node i,j,k may be different.

The magnetic-field updating coefficients are defined by material properties in the same form as before

$$H_{x1}|_{i,j,k} = \frac{1 - \bar{\rho}_{i,j,k} \Delta t / (2\mu_{i,j,k})}{1 + \bar{\rho}_{i,j,k} \Delta t / (2\mu_{i,j,k})}, \quad H_{x2}|_{i,j,k} = \frac{\Delta t / (\mu_{i,j,k} \Delta)}{1 + \bar{\rho}_{i,j,k} \Delta t / (2\mu_{i,j,k})} \quad (2-9h)$$

The same equation applies to H_{y1}, H_{y2} and to H_{z1}, H_{z2} , but the material properties at the observation node i,j,k may be different.

2.2.3 Exponential time stepping

For a medium with high loss the update coefficients in Eqs. (2-9g), (2-9h) may become negative. This leads to a numerical instability. A solution to this problem is to “pre-solve” Maxwell’s curl equations, by first finding the solution of homogeneous equations, say

$$\varepsilon \frac{\partial \vec{E}}{\partial t} = -\sigma \vec{E} \rightarrow \vec{E}_{\text{hom}}(t) = \vec{E}_{\text{hom}}^0 \exp(-\sigma t / \varepsilon) \quad (2-10a)$$

and then obtain the solution of the full equations in the form of a convolution integral. This results in the following formulas for the update coefficients, valid for both homogeneous and inhomogeneous materials [5].

$$E_{x1}|_{i,j,k} = \frac{1 - \sigma_{i,j,k} \Delta t / (2\varepsilon_{i,j,k})}{1 + \sigma_{i,j,k} \Delta t / (2\varepsilon_{i,j,k})} \rightarrow \exp(-\sigma_{i,j,k} \Delta t / \varepsilon_{i,j,k})$$

$$E_{x2}|_{i,j,k} = \frac{\Delta t / (\varepsilon_{i,j,k} \Delta)}{1 + \sigma_{i,j,k} \Delta t / (2\varepsilon_{i,j,k})} \rightarrow \frac{1}{\sigma \Delta} (1 - \exp(-\sigma_{i,j,k} \Delta t / \varepsilon_{i,j,k})) \quad (2-10b)$$

The same equation applies to E_{y1}, E_{y2} and to E_{z1}, E_{z2} , respectively, but the material properties at the observation node i,j,k may be different. Eqs. (2-10b) are equivalent to Taylor series with the first or second order of accuracy.

The magnetic-field updating coefficients are modified accordingly

$$\begin{aligned}
H_{x1}|_{i,j,k} &= \frac{1 - \bar{\rho}_{i,j,k} \Delta t / (2\mu_{i,j,k})}{1 + \bar{\rho}_{i,j,k} \Delta t / (2\mu_{i,j,k})} \rightarrow \exp(-\bar{\rho}_{i,j,k} \Delta t / \mu_{i,j,k}) \\
H_{x2}|_{i,j,k} &= \frac{\Delta t / (\mu_{i,j,k} \Delta)}{1 + \bar{\rho}_{i,j,k} \Delta t / (2\mu_{i,j,k})} \rightarrow \frac{1}{\bar{\rho} \Delta} \left(1 - \exp(-\bar{\rho}_{i,j,k} \Delta t / \mu_{i,j,k}) \right)
\end{aligned} \tag{2-10c}$$

The same equation applies to H_{y1}, H_{y2} and to H_{z1}, H_{z2} , but the material properties at the observation node i,j,k may be different. Eqs. (2-10c) are again equivalent to Taylor series with the first or second order of accuracy.

The implementation of the exponential time stepping requires care, due to the singularity of the second Eq. (2-10b) when $\sigma \rightarrow 0$. A vanishingly small conductivity value for air, that is $\sigma = 10^{-6}$ S/m, was assumed to make the second Eq. (2-10b) uniformly valid.

The exponential time stepping method may be applied to problems involving highly-conductive dielectrics – human body, salt water, Earth ground – at low and intermediate frequencies. It can be also applied to the direct modeling of metal objects by imposing a very high conductivity in the object volume.

2.3 Materials properties in FDTD

In the standard FDTD formulation, every elementary Yee cell (electric-field components along a cube edges) is filled by a homogeneous medium. Dielectric boundaries can be only located between adjacent cells, therefore, they are tangential to the electric field components – see Fig. 2-3. Simultaneously, magnetic boundaries can be only located halfway between adjacent cells, therefore they are also tangential to the magnetic field components. Fig. 2-3 shows the corresponding concept.

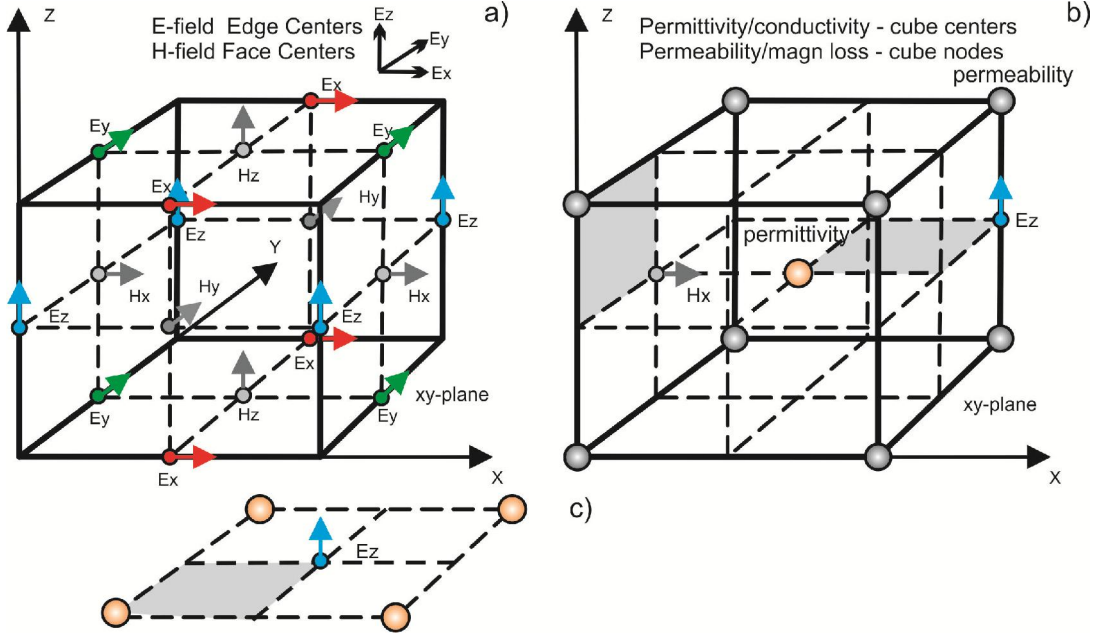


Figure 2-3 Standard field nodes and material parameter nodes. The permittivity/conductivity is defined at cell centers. The permeability/magnetic loss is defined at cell corners

Effective constitutive parameters are derived by enforcing the continuity of the tangential electric and magnetic field components in the integral formulation of the Ampere's law and Faraday's law [6]. These parameters are obtained by averaging the parameters of the neighboring cells with respect to the discontinuity. Such formulation is first-order accurate in cell size and leads to the definition of an effective permittivity and permeability. The result has the form [6], [7] :

- $\epsilon_{i,j,k}, \sigma_{i,j,k}$ in Eqs. (2-9a) are obtained by averaging *four* adjacent center-cell values
 – see Fig. 2-3c;
- $\mu_{i,j,k}, \bar{\rho}_{i,j,k}$ in Eqs. (2-9b) are obtained by averaging four adjacent node values.

2.4 Absorbing Boundary Conditions

An infinite large computation domain is generated when dealing with open space problem. Due to finite computational capacity and memory size in computer, it is however impossible to handle these problems directly. To simulate the infinite space, Absorbing Boundary Conditions (ABCs) are needed.

A wide variety of ABCs exist. In this thesis the first- and second-order ABCs due to Mur [8] augmented with Mei's superabsorption [9] will be used.

A simple yet reasonably accurate combination is that of the first-order Mur's ABCs

and superabsorption. This combination does not need a special treatment for edges and corners. It is trivially extended to the case of an inhomogeneous medium and still has a sufficient numerical accuracy (second-order) as confirmed by a number of computational examples.

2.4.1 Mur's ABCs

Mur's ABC is inspired by the idea of the boundary conditions in acoustic wave problems. Let's take a look at Fig. 2-4 that follows. First, if a source of excitation is located approximately in the center of the FDTD domain, and the size of this domain is large enough, the signal that hits the boundary can be considered as a combination of plane propagating waves.

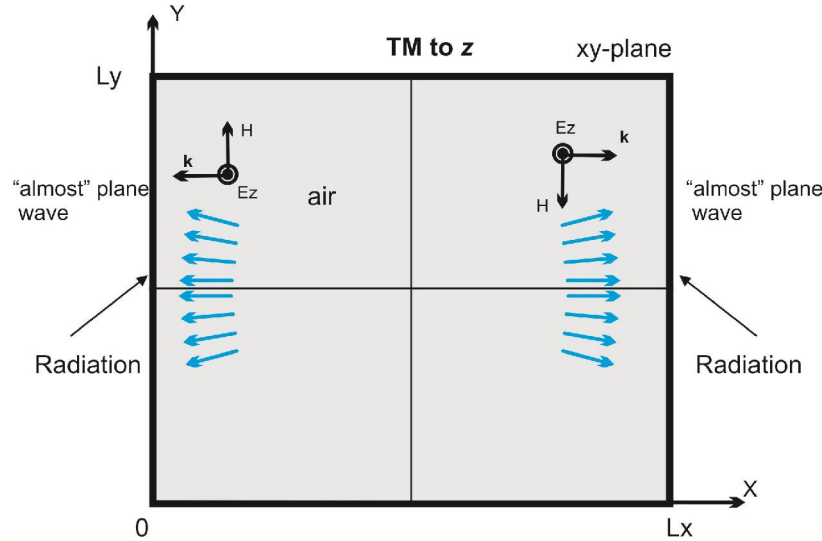


Figure 2-4 An "almost" plane wave that is coming toward the boundaries needs to be absorbed

Such a field is conventionally described in terms of the so-called parabolic approximation, which initially was developed for well-collimated weakly-diffracted optical beams - almost plane waves. Let us start with the wave equation for an arbitrary field quantity, W ,

$$\frac{\partial^2 W}{\partial t^2} - c_0^2 \left(\frac{\partial^2 W}{\partial x^2} + \frac{\partial^2 W}{\partial y^2} + \frac{\partial^2 W}{\partial z^2} \right) = 0 \quad (2-11)$$

One can obtain another form of this equation, to underscore the dominant propagation along the x-axis

$$\left(\frac{\partial}{\partial t} - c_0 \frac{\partial}{\partial x} \right) \left(\frac{\partial}{\partial t} + c_0 \frac{\partial}{\partial x} \right) W - c_0^2 \left(\frac{\partial^2 W}{\partial y^2} + \frac{\partial^2 W}{\partial z^2} \right) = 0, \quad (2-12)$$

either in the positive or in the negative direction. We are interested in the boundary at $x=0$, i.e. in the negative direction of propagation. When the direction of propagation is exactly the negative x-axis and the wave is exactly plane, from Eq. (2-12) one obtains

$$\left(\frac{\partial}{\partial t} - c_0 \frac{\partial}{\partial x}\right)W = 0 \quad (2-13)$$

While this observation is only approximately true, we could still replace one spatial derivative in the first term on the right-hand side of Eq. (2-12) by

$$\frac{\partial}{\partial t} \approx c_0 \frac{\partial}{\partial x} \Rightarrow \left(\frac{\partial}{\partial t} + c_0 \frac{\partial}{\partial x}\right) \approx 2 \frac{\partial}{\partial t} \quad (2-14)$$

This yields

$$\left(\frac{\partial}{\partial t} - c_0 \frac{\partial}{\partial x}\right)\left(2 \frac{\partial}{\partial t}\right)W - c_0^2 \left(\frac{\partial^2 W}{\partial y^2} + \frac{\partial^2 W}{\partial z^2}\right) = 0 \quad (2-15)$$

or, which may be rewritten as,

$$\frac{\partial^2 W}{\partial t^2} - c_0 \frac{\partial^2 W}{\partial t \partial x} - \frac{c_0^2}{2} \left(\frac{\partial^2 W}{\partial y^2} + \frac{\partial^2 W}{\partial z^2}\right) = 0 \quad (2-16)$$

Eq. (2-16) is the well-known parabolic approximation to the wave equation. It says that the electromagnetic signal propagates predominantly along the negative x-axis; it is also subject to diffraction in the transversal plane (in the yz-plane). The parabolic equation is easier to solve than the wave equation itself, and it is straightforward to formulate the boundary conditions in terms of it. The first-order Mur's ABCs utilize Eq. (2-13); the second-order Mur's ABCs utilize Eq. (2-16).

First-order Mur's ABCs are given by Eq. (2-13) applied at all boundaries. In particular,

$$\frac{\partial E_z}{\partial t} - c_0 \frac{\partial E_z}{\partial x} = 0 \quad (2-17a)$$

$$\frac{\partial E_z}{\partial t} + c_0 \frac{\partial E_z}{\partial x} = 0 \quad (2-17b)$$

for the left and right boundary in Fig. 2-4, respectively. The results for the lower and upper boundaries are obtained by permutation ($x \rightarrow y$). Despite this very simple nature, even those equations will do a decent job when implemented correctly.

2.4.2 Implementation of the first-order Mur's ABCs

Proceed with the first-order Mur's ABCs Eqs. (2-17). The central point is how to implement them properly at the boundaries. We will use the central differences in both the space and the time domains, so that our result will have a local truncation error of the second order in all increments. One has

$$\begin{aligned} \frac{\partial E_z}{\partial t} - c_0 \frac{\partial E_z}{\partial x} = 0 &\Rightarrow \\ \frac{1}{2} \left(\frac{E_{z1,j,k}^{n+1} - E_{z1,j,k}^n}{\Delta t} + \frac{E_{z2,j,k}^{n+1} - E_{z2,j,k}^n}{\Delta t} \right) - c_0 \frac{1}{2} \left(\frac{E_{z2,j,k}^{n+1} - E_{z1,j,k}^{n+1}}{\Delta} + \frac{E_{z2,j,k}^n - E_{z1,j,k}^n}{\Delta} \right) &= 0 \\ E_{z1,j,k}^{n+1} = E_{z2,j,k}^n + \frac{c_0 \Delta t - \Delta}{c_0 \Delta t + \Delta} (E_{z2,j,k}^{n+1} - E_{z1,j,k}^n) & \quad j = 1 : N_y + 1, \quad k = 1 : N_z \end{aligned} \quad (2-18a)$$

for the left boundary. Eq. (2-18a) is valid for any node on the boundary, including the edges and the corners. When the inhomogeneous material properties are involved, the local speed of light $c = 1/\sqrt{\mu\epsilon}$ is assumed to be constant close to the boundary in the direction perpendicular to the boundary, on both its sides. The tangential changes are allowed at any node of the boundary; they are included into consideration exactly as in the main FDTD grid. For the right boundary in Fig. 2-4, one similarly has

$$\begin{aligned} \frac{\partial E_z}{\partial t} + c_0 \frac{\partial E_z}{\partial x} = 0 &\Rightarrow \\ \frac{1}{2} \left(\frac{E_{zN_x+1,j,k}^{n+1} - E_{zN_x+1,j,k}^n}{\Delta t} + \frac{E_{zN_x,j,k}^{n+1} - E_{zN_x,j,k}^n}{\Delta t} \right) + c_0 \frac{1}{2} \left(\frac{E_{zN_x+1,j,k}^{n+1} - E_{zN_x,j,k}^{n+1}}{\Delta} + \frac{E_{zN_x+1,j,k}^n - E_{zN_x,j,k}^n}{\Delta} \right) &= 0 \\ E_{zN_x+1,j,k}^{n+1} = E_{zN_x,j,k}^n + \frac{c_0 \Delta t - \Delta}{c_0 \Delta t + \Delta} (E_{zN_x,j,k}^{n+1} - E_{zN_x+1,j,k}^n) & \quad j = 1 : N_y + 1, \quad k = 1 : N_z \end{aligned} \quad (2-18b)$$

The extensions to the lower and upper boundaries and to the 3D case are straightforward and the implementation MATLAB code list below as reference.

```

% Left
EyN(1, :, :) = EyP(2, :, :) + m1*(EyN(2, :, :) - EyP(1, :, :)); % left - Ey;
EzN(1, :, :) = EzP(2, :, :) + m1*(EzN(2, :, :) - EzP(1, :, :)); % left - Ez;

% Right
EyN(Nx+1, :, :) = EyP(Nx, :, :) + m1*(EyN(Nx, :, :) - EyP(Nx+1, :, :)); % right - Ey;
EzN(Nx+1, :, :) = EzP(Nx, :, :) + m1*(EzN(Nx, :, :) - EzP(Nx+1, :, :)); % right - Ez;

% Front
ExN(:, 1, :) = ExP(:, 2, :) + m1*(ExN(:, 2, :) - ExP(:, 1, :)); % front - Ex;
EzN(:, 1, :) = EzP(:, 2, :) + m1*(EzN(:, 2, :) - EzP(:, 1, :)); % front - Ez;

% Rear
ExN(:, Ny+1, :) = ExP(:, Ny, :) + m1*(ExN(:, Ny, :) - ExP(:, Ny+1, :)); % rear - Ex;
EzN(:, Ny+1, :) = EzP(:, Ny, :) + m1*(EzN(:, Ny, :) - EzP(:, Ny+1, :)); % rear - Ez;

% Bottom
ExN(:, :, 1) = ExP(:, :, 2) + m1*(ExN(:, :, 2) - ExP(:, :, 1)); % bottom - Ex;
EyN(:, :, 1) = EyP(:, :, 2) + m1*(EyN(:, :, 2) - EyP(:, :, 1)); % bottom - Ey;

% Top
ExN(:, :, Nz+1) = ExP(:, :, Nz) + m1*(ExN(:, :, Nz) - ExP(:, :, Nz+1)); % top - Ex;
EyN(:, :, Nz+1) = EyP(:, :, Nz) + m1*(EyN(:, :, Nz) - EyP(:, :, Nz+1)); % top - Ez;

```

2.4.3. “Superabsorption” ABCs

The Mei-Fang “superabsorption” method [9] is not an ABC by itself, but rather a numerical procedure for the improvement of the local ABC's applied to the FDTD technique [10]. It embodies an error-canceling formulation according to which the same ABC is applied to both E and H field components on and near the outer boundaries, depending on the polarization examined.

Namely, the calculation of the 2-D TM (TE) magnetic (electric) components, from their respective boundary ABC-derived electric (magnetic) ones, yields reflection errors which are strongly related to the errors in magnetic (electric) field components directly computed from the ABC. The opposite sign that these errors have in both of the above separate calculations is a point of crucial importance in the superabsorption procedure. Taking this fact into consideration and by properly combining the two different computations of the magnetic (electric) fields near the boundary, it is possible to cancel the reflection errors mutually while maintaining the correct values of the fields on the boundary [10].

Fig. 2-5 illustrates schematically the implementation of the method for the right boundary ($x=L$) of the computational domain in Fig. 2-5. For this boundary, we apply the first-order Mur’s ABC given by Eq. (2-18b) not only to the Ez-field but also to the Hy-field in the vicinity to that boundary, i.e.

$$H_{y_{N_x,j,k}}^{n+1/2(2)} = H_{y_{N_x,j,k}}^{n-1/2} + \frac{c_0 \Delta t - \Delta}{c_0 \Delta t + \Delta} \left(H_{y_{N_x-1,j}}^{n+1/2} - H_{y_{N_x,j,k}}^{n-1/2} \right) \quad (2-19a)$$

Next, we compute the Hy-field by the regular finite-difference scheme to obtain

$$H_{y_{N_x,j,k}}^{n+1/2(1)} \quad (2-19b)$$

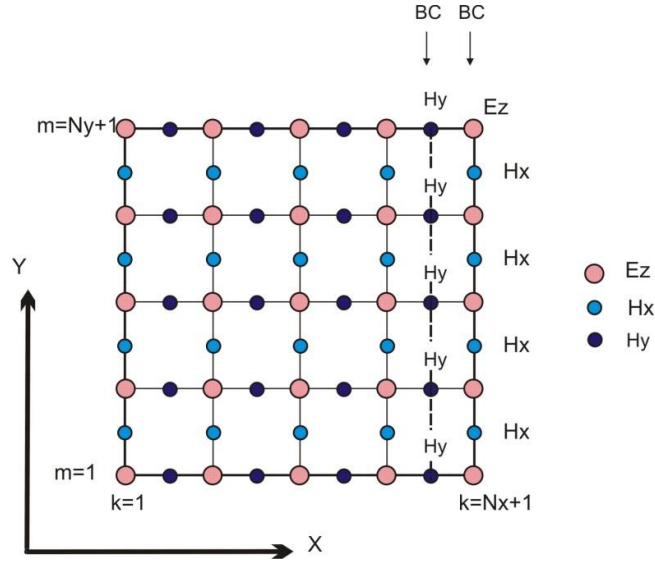


Figure 2-5 Superabsorption ABCs on the right boundary

After that, we form a weighted average of those two values and obtain the final updated magnetic field value at the last point by

$$H_{y_{N_x,j,k}}^{n+1/2} = \frac{H_{y_{N_x,j,k}}^{n+1/2(1)} + \rho H_{y_{N_x,j,k}}^{n+1/2(2)}}{1 + \rho} \quad (2-19c)$$

Here,

$$\rho = \frac{c_0 \Delta t}{\Delta} \quad (2-20)$$

The MATLAB code show below:

```
coeff1 = (c0*dt - d)/(c0*dt + d);
rho     = c0*dt/d; RHO = 1 + rho;
% Left
```

```

HyN(1, :, :) = (HyN(1, :, :) + rho*(HyP(2, :, :) + coeff1*(HyN(2, :, :) - HyP(1, :, :))))/RHO; %
left - Hy;
HzN(1, :, :) = (HzN(1, :, :) + rho*(HzP(2, :, :) + coeff1*(HzN(2, :, :) - HzP(1, :, :))))/RHO; %
left - Hz;
% Right
HyN(Nx, :, :) = (HyN(Nx, :, :) + rho*(HyP(Nx-1, :, :) + coeff1*(HyN(Nx-1, :, :) -
HyP(Nx, :, :))))/RHO; % right - Hy;
HzN(Nx, :, :) = (HzN(Nx, :, :) + rho*(HzP(Nx-1, :, :) + coeff1*(HzN(Nx-1, :, :) -
HzP(Nx, :, :))))/RHO; % right - Hz;
% Front
HxN(:, 1, :) = (HxN(:, 1, :) + rho*(HxP(:, 2, :) + coeff1*(HxN(:, 2, :) - HxP(:, 1, :))))/RHO; %
front - Hx;
HzN(:, 1, :) = (HzN(:, 1, :) + rho*(HzP(:, 2, :) + coeff1*(HzN(:, 2, :) - HzP(:, 1, :))))/RHO; %
right - Hz;
% Rear
HxN(:, Ny, :) = (HxN(:, Ny, :) + rho*(HxP(:, Ny-1, :) + coeff1*(HxN(:, Ny-1, :) -
HxP(:, Ny, :))))/RHO; % rear - Hx;
HzN(:, Ny, :) = (HzN(:, Ny, :) + rho*(HzP(:, Ny-1, :) + coeff1*(HzN(:, Ny-1, :) -
HzP(:, Ny, :))))/RHO; % rear - Hz;
% Bottom
HxN(:, :, 1) = (HxN(:, :, 1) + rho*(HxP(:, :, 2) + coeff1*(HxN(:, :, 2) - HxP(:, :, 1))))/RHO; %
bottom - Hx;
HyN(:, :, 1) = (HyN(:, :, 1) + rho*(HyP(:, :, 2) + coeff1*(HyN(:, :, 2) - HyP(:, :, 1))))/RHO; %
bottom - Hy;
% Top
HxN(:, :, Nz) = (HxN(:, :, Nz) + rho*(HxP(:, :, Nz-1) + coeff1*(HxN(:, :, Nz-1) -
HxP(:, :, Nz))))/RHO; % top - Hx;
HyN(:, :, Nz) = (HyN(:, :, Nz) + rho*(HyP(:, :, Nz-1) + coeff1*(HyN(:, :, Nz-1) -
HyP(:, :, Nz))))/RHO; % top - Hy;

```

It can be shown that this procedure significantly decreases the error of a local ABC, in particular, the first-order Mur's ABC. It is also very simply implemented and does not require any extra variables. When the inhomogeneous material properties are involved, the same scheme is followed as for the first-order Mur's ABCs.

2.5 Perfectly Matched Layer (PML)

In an actual engineering environment, when testing the performance of microwave and RF devices, the interference from reflection and refraction should be avoided. There are however no large enough space available in most cases. An anechoic chamber may be built to simulate an infinitely large space by using wave-absorbing materials. The PML in numerical method is an analogy of the chamber. The idea of the PML is different from ABCs – rather than analytically cancelling the field, the PML absorbs the energy as it passes through additional material layers.

The PML was first discovered by J.-P. Bérenger [11] and extensively tested by Allen Taflove and co-workers - see Refs. [2], [12], [13]. Only one year after the initial series of fundamental papers [11] [12] [13], Sacks et al [14] published an independent model of the PML, the so-called anisotropic or unsplit PML, which quickly became the de facto standard not only for FDTD simulations but also in the finite-element method [15] [14] [16]. Here, we will discuss the original Bérenger's PML only.

For simplicity, we start with the 2D field case, with the TE to z field shown in Fig. 2-6 that follows. The magnetic field in this case is always directed along the z -axis, but the propagation direction (wave vector) is always in the xy -plane.

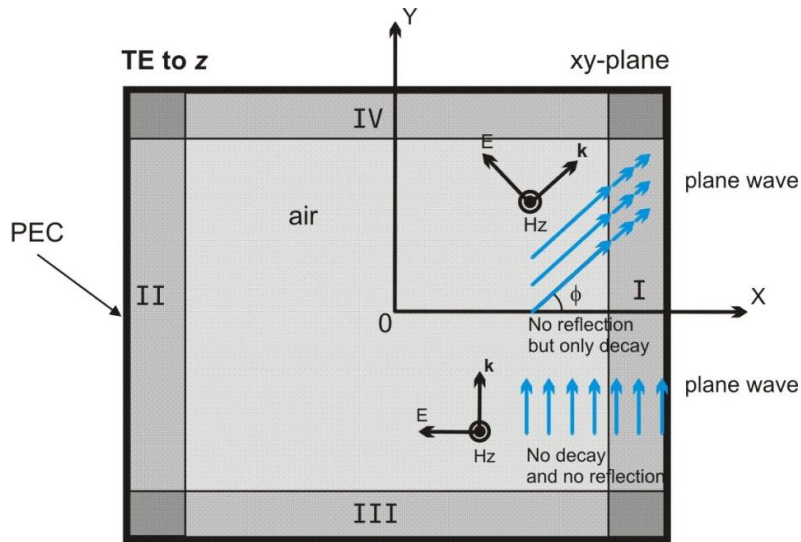


Figure 2-6 The PML concept for the TE to z field

The PML in Fig. 2-6 should satisfy two conditions:

1. Absorb a plane wave at any incidence angle, without reflection at the PML boundary. Absorption and reflectionless behavior incidence angle initiated the word "perfectly" in the PML abbreviation. The incidence must not be exactly oblique.
2. Do not absorb and do not perturb any plane wave at exactly oblique incidence -see Fig. 2-6.

The latter condition is conventionally satisfied if we terminate the PML into a PEC boundary, that is a perfect electric conductor shown in Fig. 2-6.

The TM to z case is very similar, as shown in Fig. 2-7, The electric field in this case is always directed along the z -axis, but the propagation direction (wave vector) is again always in the xy -plane.

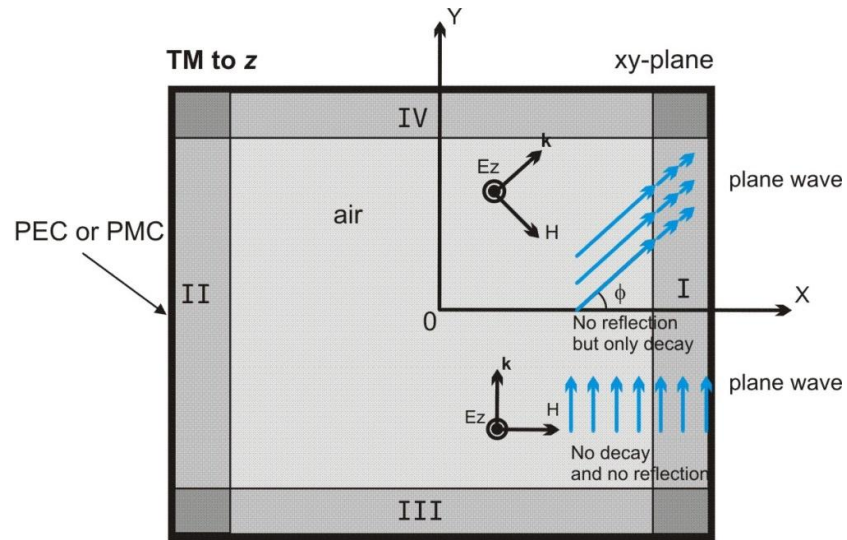


Figure 2-7 The PML concept for the TM to z field

If we require both conditions 1 and 2 to be satisfied, then it is seen from the geometry of Fig. 2-7 that a PEC boundary of the PML will disturb the solution at oblique incidence. The Perfect Magnetic Conductor (PMC) boundary or the radiation boundary should be actually more adequate for this case. If the wave signal at oblique incidences is not present or is not important, the difference between the boundaries is not significant. Both boundaries can be equally simply implemented in the FDTD method.

In all distinct PML regions shown in Fig. 2-6 and Fig. 2-7 the loss parameters of an artificial lossy media will be different, irrespective of the particular PML model used, see Fig 2-8. In fact, the PML was first carefully formulated for the TE case in Fig. 2-6, by assigning those distinct parameters.

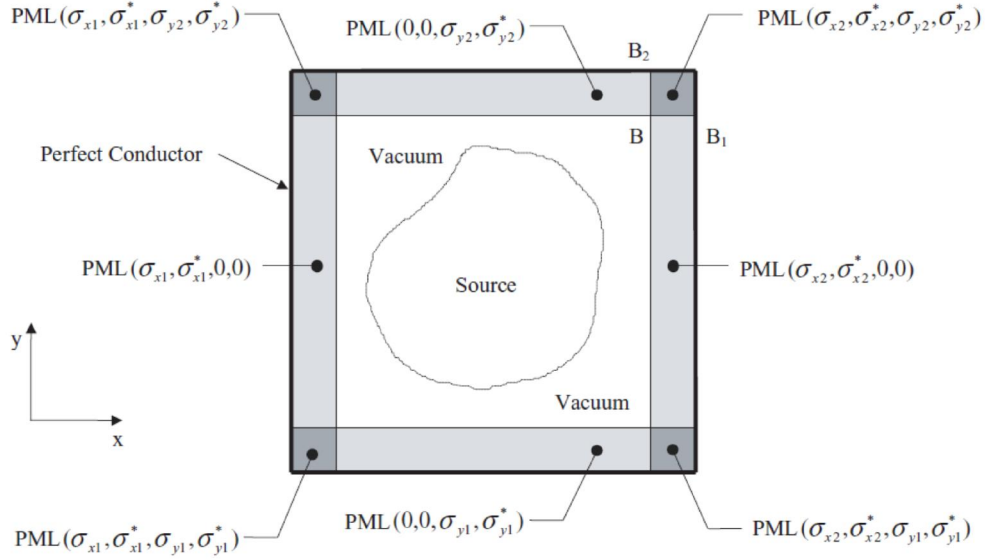


Figure 2-8 different conductivity in different PML regions

The PML boundary condition is a lossy material boundary layer that is perfectly matched to the physical solution space. In the original Bérenger's model [11], [17], [18] this is achieved through a “field splitting” of the electric and magnetic field intensities, leading to a modified set of Maxwell's equations. It has been shown that an arbitrarily polarized wave incident on this PML medium is perfectly transmitted and has the same phase velocity and characteristic wave impedance as the incident wave while attenuating rapidly along the normal axis. Bérenger's PML method has been successfully implemented within the FDTD algorithm [16].

For example, the Maxwell's equations for TM to z field can be split into four equations in PML region [11]:

$$\begin{aligned}
 \frac{\partial E_z}{\partial t} &= \frac{1}{\epsilon} \frac{\partial H_y}{\partial x} - \frac{1}{\epsilon} \frac{\partial H_x}{\partial y} - \frac{\sigma}{\epsilon} E_z & \frac{\partial E_{zx}}{\partial t} &= \frac{1}{\epsilon} \frac{\partial H_y}{\partial x} - \frac{\sigma_x}{\epsilon} E_{zx} \\
 \frac{\partial H_x}{\partial t} &= -\frac{1}{\mu} \frac{\partial E_z}{\partial y} - \frac{\sigma^*}{\mu} H_x & \frac{\partial E_{zy}}{\partial t} &= -\frac{1}{\epsilon} \frac{\partial H_x}{\partial y} - \frac{\sigma_y}{\epsilon} E_{zy} \\
 \frac{\partial H_y}{\partial t} &= \frac{1}{\mu} \frac{\partial E_z}{\partial x} - \frac{\sigma^*}{\mu} H_y & \frac{\partial H_x}{\partial t} &= -\frac{1}{\mu} \frac{\partial (E_{zx} + E_{zy})}{\partial y} - \frac{\sigma_y^*}{\mu} H_x \\
 & & \frac{\partial H_y}{\partial t} &= \frac{1}{\mu} \frac{\partial (E_{zx} + E_{zy})}{\partial x} - \frac{\sigma_x^*}{\mu} H_y
 \end{aligned} \Rightarrow$$

(2-21)

by splitting the electric field into two independent subcomponents, $E_z \rightarrow E_{zx} + E_{zy}$

in the PML region. The Maxwell's equations themselves give no reflection at the boundary at normal incidence if [2],

$$\frac{\sigma}{\varepsilon} = \frac{\sigma^*}{\mu} \quad (2-22)$$

However, the reflection at other incidence angles will still be present. On the other hand, their counterpart from Eqs. (2-21), which matches to the original Maxwell's equations at the boundary where

$$E_z = E_{zx} + E_{zy} \quad (2-23)$$

gives no reflections and satisfies conditions 1 and 2 for the PML by a proper choice of artificial conductivities $\sigma_{x,y}, \sigma_{x,y}^*$. In particular, in both domains I and II in Fig. 2-6 and 2-7, only two losses are present [11]

$$\frac{\sigma_x}{\varepsilon} = \frac{\sigma_x^*}{\mu} \neq 0, \quad \sigma_y = \sigma_y^* = 0 \quad (2-24a)$$

Similarly, in both domains III and IV in Figs. 2-6, 2-7

$$\frac{\sigma_y}{\varepsilon} = \frac{\sigma_y^*}{\mu} \neq 0, \quad \sigma_x = \sigma_x^* = 0 \quad (2-24b)$$

At the four corners of the PML, where there is overlap of two subdomains [11], all four losses are present, i.e.

$$\frac{\sigma_x}{\varepsilon} = \frac{\sigma_x^*}{\mu} \neq 0, \quad \frac{\sigma_y}{\varepsilon} = \frac{\sigma_y^*}{\mu} \neq 0 \quad (2-24c)$$

This is done to match the PML subdomains to each other. A similar scheme is used in the general 3D case [17].

"Standard" quadratic Bérenger's conductivity profile is defined as [11] [15]:

$$\sigma = \sigma_{\max} \left(\frac{r}{R_{\text{PML}}} \right)^n, \quad n = 2, \quad \frac{\sigma}{\varepsilon} = \frac{\sigma^*}{\mu} \quad (2-25)$$

Where R_{PML} is PML thickness. If a constant conductivity over the layer is employed, the FDTD reflection coefficient cannot be smaller than 3% [11]. This value decreases to 0.1% for a linear profile, and to 0.01% for a quadratic profile.

Finally, the reflection coefficient is given by

$$R = \exp\left(-\frac{2}{n+1} \frac{\sigma_{\max} R_{\text{PML}}}{\epsilon c_0}\right) \quad (2-26)$$

Interestingly enough, the reflection coefficient only depends on PML thickness, not the number of cells within the PML. This means that the PML should theoretically work for any number of cells; a practical value is, however, about 10-15. The optimum values for the reflection coefficient are 10^{-5} to 10^{-6} [11].

Despite some initial complexity, the practical FDTD implementation is straightforward and it is described in detail in Refs. [11], [17]. For the 2D case, three fields are updated marching on in time in the internal region, and four fields in the PML region, respectively; see Fig 2-9. However, In 3D case, the complexity increase exponentially with 26 regions to deal with, see Fig 2-10.

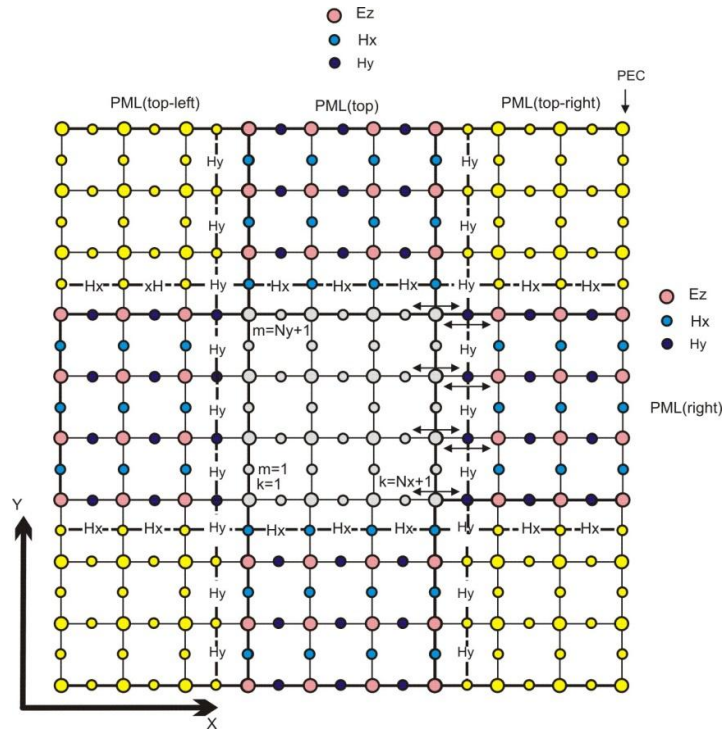


Figure 2-9 A sketch of one 2D PML grid with sides and corners

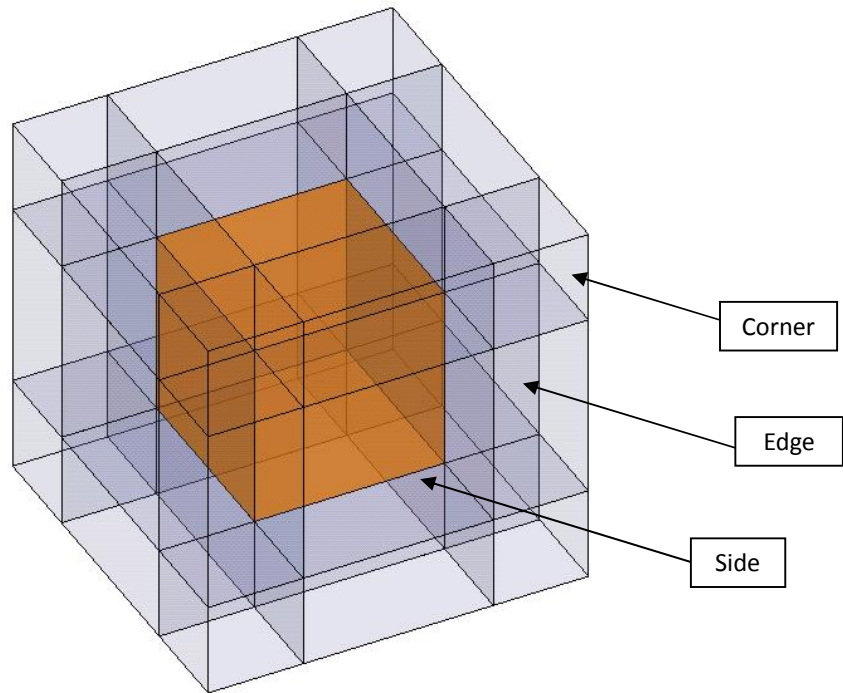


Figure 2-10 3D PML regions - 6 Sides, 12 Edges and 8 Corners

CHAPTER 3

COINCIDENT PHASE CENTER ANTENNA

3.1 Electric dipole model

3.1.1 Standard small dipole model

A small dipole antenna is represented by a uniform line current, $i_s(t)$, which flows over a length l . The length l is usually much smaller than the cell size. The current is centered at the corresponding electric field node as shown in Fig. 3-1 [19].

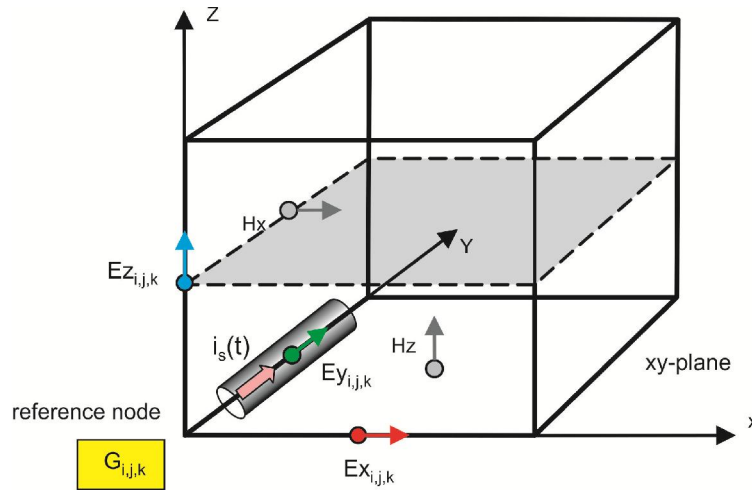


Figure 3-1 Dipole antenna with the impressed line current $i_s(t)$

The line current is transformed to an equivalent volumetric current density averaged over one unit cell:

$$J_s(t) = \frac{l}{\Delta^3} i_s(t) \quad (3-1)$$

which produces the same electric dipole moment. This current density is substituted in one of the FDTD update equations for the electric field (see Eqs. (2-9d) to (2-9f)). For the dipole shown in Fig. 3-1, the result has the form

$$E_y^{n+1}(i, j, k) = E_{y1} E_y^n(i, j, k) + E_{y2} \times \left(H_x^{n+1/2}(i, j, k) - H_x^{n+1/2}(i, j, k-1) + H_z^{n+1/2}(i-1, j, k) - H_z^{n+1/2}(i, j, k) - \Delta J_s^{n+1/2} \right) \quad (3-2)$$

where

$$E_{y1} = \frac{1 - \sigma\Delta t / (\epsilon\Delta)}{1 + \sigma\Delta t / (2\epsilon)}, \quad E_{y2}|_{i,j,k} = \frac{\Delta t / (\epsilon\Delta)}{1 + \sigma\Delta t / (2\epsilon)} \quad (3-3)$$

An important observation is that it is very straightforward to implement Eqs. (3-2) in practice. Namely, only current excitation terms have to be added after the standard update equations for the electric field.

3.1.2 Coincident Phase Centers dipole model for arbitrary orientation

For an arbitrarily oriented dipole, with the unit direction vector \vec{n} , one could consider a superposition solution in the form of three orthogonal elementary dipoles oriented along the x-, y-, and z-axes. However, their phase centers will not be coincident – see Fig. 3-1 for an illustration. A modification of the model can be made that is shown in Fig. 3-2. Here, the dipole source is effectively placed at the corner node of the Yee cell. Two adjacent electric field nodes acquire the half of the dipole current.

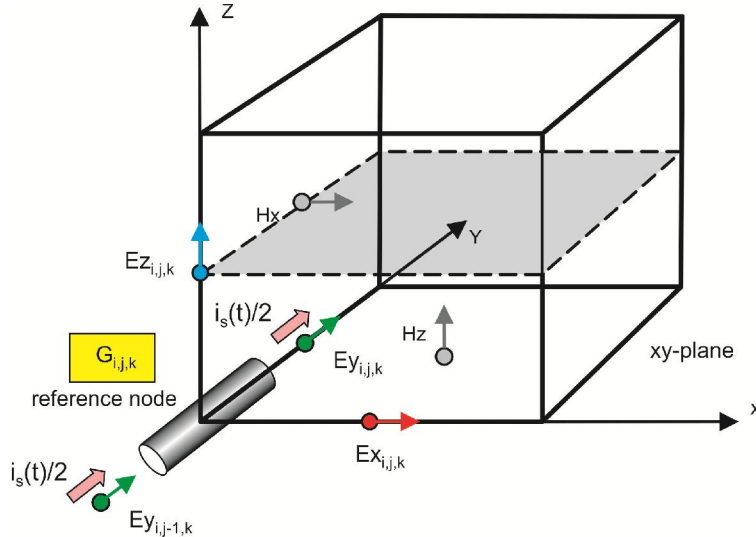


Figure 3-2 Dipole antenna model with the dipole placed at the center node of the Yee cell

The dipole of arbitrary orientation with the unit direction vector \vec{n} is then considered as a superposition of three dipoles directed along the x-, y-, and z-axes. All those dipoles have the same (phase) center. The corresponding current densities are given by

$$J_{sx}(t) = \frac{1}{2} n_x J_s(t), \quad J_{sy}(t) = \frac{1}{2} n_y J_s(t), \quad J_{sz}(t) = \frac{1}{2} n_z J_s(t) \quad (3-4)$$

The above model may be treated as a symmetric point source model.

The port update given Eq. (3-2) is straightforwardly modified to the present case: it remains the same for the node i, j, k (except that the current is divided by two), and uses index substitution $j \rightarrow j-1$ for the second node in Fig. 3-2.

Complete update equations for a dipole of arbitrary orientation have the form

$$\begin{aligned}
 E_x^{n+1}(i, j, k) &\rightarrow E_x^{n+1}(i, j, k) - E_{x2}(0.5\Delta n_z J_s^{n+1/2}) \\
 E_x^{n+1}(i-1, j, k) &\rightarrow E_x^{n+1}(i-1, j, k) - E_{x2}(0.5\Delta n_z J_s^{n+1/2}) \\
 E_y^{n+1}(i, j, k) &\rightarrow E_y^{n+1}(i, j, k) - E_{y2}(0.5\Delta n_y J_s^{n+1/2}) \\
 E_y^{n+1}(i, j-1, k) &\rightarrow E_y^{n+1}(i, j-1, k) - E_{y2}(0.5\Delta n_y J_s^{n+1/2}) \\
 E_z^{n+1}(i, j, k) &\rightarrow E_z^{n+1}(i, j, k) - E_{z2}(0.5\Delta n_z J_s^{n+1/2}) \\
 E_z^{n+1}(i, j, k-1) &\rightarrow E_z^{n+1}(i, j, k-1) - E_{z2}(0.5\Delta n_z J_s^{n+1/2})
 \end{aligned} \tag{3-5}$$

Here, only current excitation terms have to be added after the standard update equations for the electric field. The MATLAB implementation is really straightforward as:

```

% setting up parameters
Js = PortM(m)/d^3*(IG(m, kt)+IG(m, kt+1))/2; % volumetric current density at
n+1/2 - tested
i_e = PortIndX(m); % port location grid nodes
j_e = PortIndY(m); % port location grid nodes
k_e = PortIndZ(m); % port location grid nodes
Jx = d*Js/2*PortNX(m);
Jy = d*Js/2*PortNY(m);
Jz = d*Js/2*PortNZ(m);

ExN(i_e, j_e, k_e) = ExN(i_e, j_e, k_e) - Ex2(i_e, j_e-1, k_e-1)*Jx;
ExN(i_e-1, j_e, k_e) = ExN(i_e-1, j_e, k_e) - Ex2(i_e-1, j_e-1, k_e-1)*Jx;

EyN(i_e, j_e, k_e) = EyN(i_e, j_e, k_e) - Ey2(i_e-1, j_e, k_e-1)*Jy;
EyN(i_e, j_e-1, k_e) = EyN(i_e, j_e-1, k_e) - Ey2(i_e-1, j_e-1, k_e-1)*Jy;

EzN(i_e, j_e, k_e) = EzN(i_e, j_e, k_e) - Ez2(i_e-1, j_e-1, k_e)*Jz;
EzN(i_e, j_e, k_e-1) = EzN(i_e, j_e, k_e-1) - Ez2(i_e-1, j_e-1, k_e-1)*Jz;

AntI(m, kt) = IG(m, kt);

AntE(m, kt) = PortNX(m)*(Exp(i_e, j_e, k_e) + Exp(i_e-1, j_e, k_e)) + ...
PortNY(m)*(Exp(i_e, j_e, k_e) + Exp(i_e, j_e-1, k_e)) + ...

```

```

        PortNZ(m)*(EzP(i_e, j_e, k_e) + EzP(i_e, j_e, k_e-1));
AntE(m, kt) = AntE(m, kt)/2;

Anth(m, kt) = PortNX(m)*(HxN(i_e, j_e, k_e) + HxN(i_e, j_e-1, k_e) + HxN(i_e,
j_e, k_e-1) + HxN(i_e, j_e-1, k_e-1)) + ...
        PortNY(m)*(HyN(i_e, j_e, k_e) + HyN(i_e-1, j_e, k_e) + HyN(i_e, j_e,
k_e-1) + HyN(i_e-1, j_e, k_e-1)) + ...
        PortNZ(m)*(HzN(i_e, j_e, k_e) + HzN(i_e-1, j_e, k_e) + HzN(i_e, j_e-1,
k_e) + HzN(i_e-1, j_e-1, k_e)) + ...
        PortNX(m)*(HxP(i_e, j_e, k_e) + HxP(i_e, j_e-1, k_e) + HxP(i_e, j_e,
k_e-1) + HxP(i_e, j_e-1, k_e-1)) + ...
        PortNY(m)*(HyP(i_e, j_e, k_e) + HyP(i_e-1, j_e, k_e) + HyP(i_e, j_e,
k_e-1) + HyP(i_e-1, j_e, k_e-1)) + ...
        PortNZ(m)*(HzP(i_e, j_e, k_e) + HzP(i_e-1, j_e, k_e) + HzP(i_e, j_e-1,
k_e) + HzP(i_e-1, j_e-1, k_e));

Anth(m, kt) = Anth(m, kt)/8;

```

The advantage of this model described by the code above is the ability to characterize the dipole of arbitrary orientation, while keeping the same phase center. Its disadvantage is a relatively “large” volume occupied by the dipole model that extends to two unit cells in every direction.

3.2 Magnetic dipole (coil antenna) model

3.2.1 General facts about coil antennas

A magnetic dipole is equivalent to a small coil antenna. Consider a coil antenna with the dimensions shown in Fig. 3-3. The antenna has N turns; the coil cross-section area is A ; the length is l . The antenna is oriented along the z -axis. The coil may have a finite magnetic core.

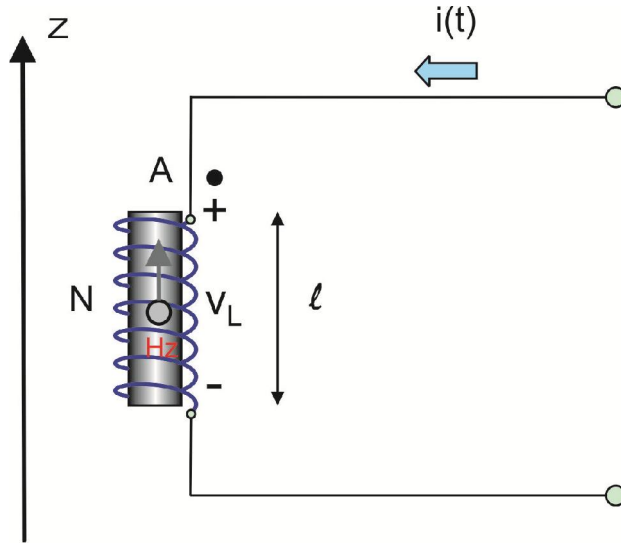


Figure 3-3 A coil antenna (with or without) the magnetic core

The antenna is excited by a current pulse $i(t)$. If necessary, the voltage across the coil antenna may be calculated as [20],

$$v_L(t) = L \frac{di}{dt} + Ri, \quad L = L_{\text{static}}, \quad R = R_{\text{static}} + R_{\text{rad}} \quad (3-6)$$

where two indexes relate to static values and their radiation corrections, respectively. One has for the static inductance of an air-core solenoid with radius r , cross-section area A , and length l ,

$$L_{\text{static}} = \frac{\mu_0 AN^2}{l} \left(1 - \frac{8w}{3\pi} + \frac{w^2}{2} - \frac{w^4}{4} \right), \quad w = \frac{r}{l} < 1 \quad (3-7)$$

The radiation resistance is given below [20]

$$R_{\text{rad}} = \frac{\eta_0}{6\pi} \left(\frac{\omega}{c_0} \right)^4 (AN)^2 \quad (3-8)$$

The radiation resistance is negligibly small for very small coils.

The calculation of inductance for the coil with a straight magnetic core becomes a nontrivial theoretical exercise. The graphical data is given in [20]. We also present here a useful theoretical result. It is only valid for a high-permeability magnetic core, with approximately $\mu \geq 100 \mu_0$. The resulting inductance for the inductor in Fig.

3-3 has the form [21]

$$L = \frac{0.5\pi\mu_0 l^* N^2}{\ln\left[\frac{l^*}{r} - 1\right]} \left(1 - \frac{l}{2l^*}\right) \quad [\text{H}] \quad (3-9)$$

where l^* is the core length and r is the coil radius. Interestingly, the resulting inductance does not explicitly depend on the specific value of μ as long as this value is sufficiently large. More precisely, Eq. (3-9) holds only for situations where the core length-to-diameter ratio is considerably smaller than the relative magnetic permeability, $\mu_r = \mu / \mu_0$. Eq. (3-9) was compared with experimental results and indicated about 40% accuracy in predicting the inductance.

3.2.2 Receive Coil

3.2.2.1 Coil without magnetic core

In the receiving mode, the open-circuited air-core RX coil shown in Fig. 3-3 generates the induced emf voltage,

$$E_{emf}(t) = -\mu_0 AN \frac{\partial H_z}{\partial t} \quad (3-10a)$$

where the emf polarity “+” corresponds to the dotted terminal of the coil shown in Fig. 3-3. Thus, the receive coil in the open-circuit mode does not significantly disturb the incident field and acts similar to a field probe. It is an important concept when implementing the FDTD code, which means the small receive coil doesn’t need a dedicated model and reduces the complexity.

In terms of finite differences, one has

$$E_{emf}^n = -\frac{\mu_0 AN}{\Delta t} (H_z^{n+1/2}(i, j, k) - H_z^{n-1/2}(i, j, k)) \quad (3-10b)$$

An alternative is to use Eq. (2-1b) which is the Faraday’s law with zero sources; this yields

$$E_{emf}(t) = AN (\nabla \times \vec{E})_z \Rightarrow E_{emf}^n = AN (\nabla \times \vec{E})_z^n \quad (3-10c)$$

The Yee-grid discretization gives

$$\left(\nabla \times \vec{E}\right)_z^n = -1/(\Delta)\left(E_x^n(i, j+1, k) - E_x^n(i, j, k) + E_y^n(i, j, k) - E_y^n(i+1, j, k)\right) \quad (3-10d)$$

3.2.2.2 Coil with arbitrary orientation

In this case, Eq. (3-10) is modified to

$$E_{emf}(t) = -\mu_0 AN \frac{\partial \vec{H}}{\partial t} \cdot \vec{n} = -\mu_0 AN \frac{\partial \vec{H} \cdot \vec{n}}{\partial t} \quad (3-11)$$

where \vec{n} is the unit vector in the direction of the coil axis, directed toward the dotted terminal of the coil in Fig. 3-3. Eqs. (3-10b) through (3-10c) may be modified accordingly.

3.2.2.3. Coil with a magnetic core

For the coil with the core, the situation complicates. Comparing Eq. (3-7) (with $w \rightarrow 0$) and Eq. (3-9) one could in principle define the “effective” permeability within the coil, i.e. the permeability, which gives the same inductance, in the form,

$$\mu_{eff} = \frac{0.5\mu_0 l^* l}{\ln\left[\frac{l^*}{r} - 1\right] r^2} \left(1 - \frac{l}{2l^*}\right) \quad (3-12)$$

Herewith, the induced emf voltage might be defined in the form

$$E_{emf}(t) = -\mu_{eff} AN \frac{\partial \vec{H} \cdot \vec{n}}{\partial t} \quad (3-13)$$

Eq. (3-13) was not tested by comparison with experiment and should be used with care.

3.2.3 Transmit coil - a magnetic dipole

3.2.3.1 Magnetic dipole

A small transmit coil antenna which carries the current $i(t)$ in Fig. 3-3 is modeled

as an infinitesimally small magnetic dipole with a magnetic moment $M_z(t)$. For the coil without the magnetic core,

$$M_z(t) = AN i(t) \quad (3-14)$$

where A is the coil cross-section, N is the number of turns, and $i(t)$ is the instantaneous coil current. The meaning of the magnetic moment originates from the torque exerted on a loop of current in an external magnetic field. On the other hand, the magnetic moment is the only characteristic of a very small coil antenna that defines both its near- and far field [19] [22]. Generally, the magnetic moment is a vector quantity, with the unit direction vector \vec{n} . The magnetic moment is directed along the coil axis according to the right-hand rule for the electric current. For example, it is directed up in Fig. 3-3.

3.2.3.2 Magnetic dipole model with a magnetic current source

The simplest way to model the coil antenna is to introduce the magnetic current source density into Faraday's law Eq. (2-1b)

$$\mu \frac{\partial \vec{H}}{\partial t} = -\nabla \times \vec{E} - \vec{J}_m - \vec{n} J_{ms} \quad (3-15)$$

$$J_{ms}(\vec{r}, t) = \mu_0 \delta(\vec{r}) \frac{dM_z}{dt} \quad (3-16)$$

Averaging over the volume of the FDTD unit cell yields

$$J_{ms}(t) = \frac{\mu_0}{\Delta^3} \frac{dM_z}{dt} = \frac{\mu_0 AN}{\Delta^3} \frac{di}{dt} \quad (3-17)$$

The Yee-grid discretization yields

$$H_z^{n+1/2}(i, j, k) = H_z^{n-1/2}(i, j, k) + \Delta t / (\mu_0 \Delta) \left(E_x^n(i, j+1, k) - E_x^n(i, j, k) + E_y^n(i, j, k) - E_y^n(i+1, j, k) \right) - \frac{AN}{\Delta^3} \left(i^{n+1/2} - i^{n-1/2} \right) \quad (3-18)$$

This method has a number of disadvantages. One of them is that the magnetic current source given by Eqs. (3-17) and (3-18) does not work well on the boundary between

vacuum and a magnetic material. Therefore, it is not implemented in the code.

3.2.3.3 Magnetic dipole model with a loop of electric current

The small coil antenna may be modeled with a loop of electric current – see Fig. 3-4. The coil antenna is placed at the node of the co-polar magnetic field as shown in Fig. 2-1. This is not the sub-cell model of the coil, but rather the cell model.

Such a location is convenient, but it does not allow us to consider an arbitrary coil antenna orientation in general. An arbitrarily-oriented radiating coil may be considered as a superposition of three coils oriented along the axes; however, these coils will not have the same phase center.

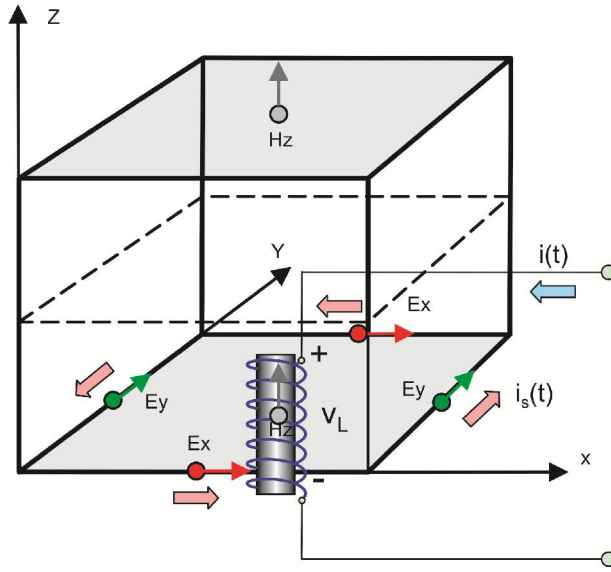


Figure 3-4 Coil antenna modeled with a loop of an equivalent electric current

By following the approach from Ref. [19], **Error! Reference source not found.** the coil in Fig. 3-4 is replaced by a square loop of the grid-aligned current $i_s(t)$ which possesses the same magnetic moment:

$$\Delta^2 i_s(t) = M_z(t) \Rightarrow i_s(t) = \frac{AN}{\Delta^2} i(t) \quad (3-19)$$

where Δ is the cell size of the cubic grid. Further, the current $i_s(t)$ is replaced by its current density uniformly distributed over every involved cell's cross-section,

$$J_s(t) = \frac{i_s(t)}{\Delta^2} \Rightarrow J_s(t) = \frac{AN}{\Delta^4} i(t) \quad (3-20)$$

Let's assume the coil is located at the H_z -field node i,j,k – see Fig. 3-4. Maxwell's equations in a lossy inhomogeneous medium for four surrounding E-field nodes

$$\varepsilon \frac{\partial \vec{E}}{\partial t} = \nabla \times \vec{H} - \sigma \vec{E} - \hat{z} J_s \quad (3-21)$$

on the Yee grid are modified to

$$E_x^{n+1}(i, j, k) = E_{x1} E_x^n(i, j, k) + E_{x2} \times \left(H_z^{n+1/2}(i, j, k) - H_z^{n+1/2}(i, j-1, k) + H_y^{n+1/2}(i, j, k-1) - H_y^{n+1/2}(i, j, k) - \Delta J_s^{n+1/2} \right) \quad (3-22a)$$

$$E_x^{n+1}(i, j+1, k) = E_{x1} E_x^n(i, j+1, k) + E_{x2} \times \left(H_z^{n+1/2}(i, j+1, k) - H_z^{n+1/2}(i, j, k) + H_y^{n+1/2}(i, j+1, k-1) - H_y^{n+1/2}(i, j+1, k) + \Delta J_s^{n+1/2} \right) \quad (3-22b)$$

$$E_y^{n+1}(i, j, k) = E_{y1} E_y^n(i, j, k) + E_{y2} \times \left(H_x^{n+1/2}(i, j, k) - H_x^{n+1/2}(i, j, k-1) + H_z^{n+1/2}(i-1, j, k) - H_z^{n+1/2}(i, j, k) + \Delta J_s^{n+1/2} \right) \quad (3-22c)$$

$$E_y^{n+1}(i+1, j, k) = E_{y1} E_y^n(i+1, j, k) + E_{y2} \times \left(H_x^{n+1/2}(i+1, j, k) - H_x^{n+1/2}(i+1, j, k-1) + H_z^{n+1/2}(i, j, k) - H_z^{n+1/2}(i+1, j, k) - \Delta J_s^{n+1/2} \right) \quad (3-22d)$$

where

$$E_{x1} = \frac{1 - \sigma \Delta t / (\varepsilon \Delta)}{1 + \sigma \Delta t / (2\varepsilon)}, \quad E_{x2}|_{i,j,k} = \frac{\Delta t / (\varepsilon \Delta)}{1 + \sigma \Delta t / (2\varepsilon)} \quad (3-23)$$

at the locations of the E-field nodes. Here, σ is the electric conductivity.

An important observation is that it is very straightforward to implement Eqs. (3-22) in practice. Namely, only current excitation terms have to be added after the standard update equations for the electric field.

3.2.3.4 Magnetic dipole model with Coincident Phase Centers for arbitrary coil orientation

The current-loop model of Fig. 3-4 is straightforwardly modified for the case of arbitrary coil orientation. The concept is shown in Fig. 3-5 that follows. The coil antenna is now placed at the center of the Yee cell. The coil in Fig. 3-5 is replaced by two square loops of the grid-aligned electric current, which in sum possess the same magnetic moment. Instead of Eq. (3-20), the current density for each loop becomes

$$J_s(t) = \frac{1}{2} \frac{AN}{\Delta^4} i(t) \quad (3-24)$$

i.e. the half of the original current density. Update Eqs. (3-22) are straightforwardly modified to the present case: they remain the same for the lower face in Fig. 3-5 and use index substitution $k \rightarrow k + 1$ for the upper face.

The coil of arbitrary orientation with the unit direction vector \vec{n} is considered as a superposition of three coils directed along the x-, y-, and z-axes. The corresponding current densities are given by

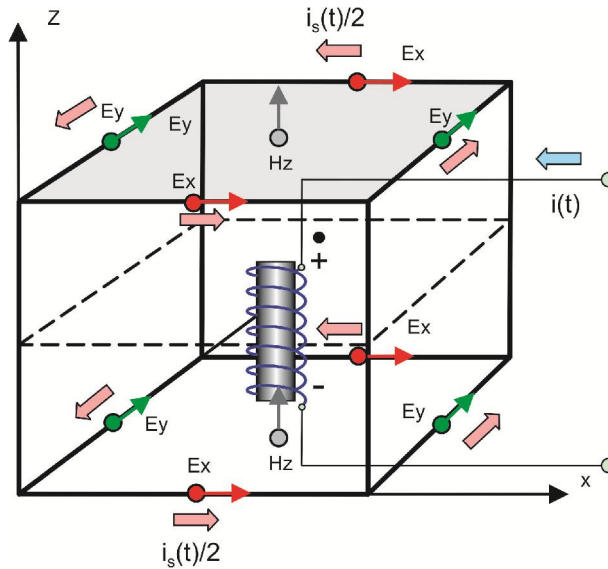


Figure 3-5 Coil antenna model with the coil placed at the center node of the Yee cell

$$J_{sx}(t) = \frac{1}{2} n_x \frac{AN}{\Delta^4} i(t), \quad J_{sy}(t) = \frac{1}{2} n_y \frac{AN}{\Delta^4} i(t), \quad J_{sz}(t) = \frac{1}{2} n_z \frac{AN}{\Delta^4} i(t) \quad (3-25)$$

All the current densities should follow the right-hand rule with regard to all three Cartesian axes as shown in Fig. 3-5 for the z-axis.

```

% setting up parameters
Js = PortM(m)/d^4*(IG(m, kt)+IG(m, kt+1))/2; % volumetric current density at
n+1/2 - tested
i_e = PortIndX(m); % port location grid nodes
j_e = PortIndY(m); % port location grid nodes
k_e = PortIndZ(m); % port location grid nodes
Jx = d*Js/2*PortNX(m);
Jy = d*Js/2*PortNY(m);
Jz = d*Js/2*PortNZ(m);

% coil/loop along the x-axis
% Update equations (simple addition - right-hand rule exactly)
EzN(i_e, j_e, k_e) = EzN(i_e, j_e, k_e) + Ez2(i_e-1, j_e-1, k_e)*Jx;
EzN(i_e, j_e+1, k_e) = EzN(i_e, j_e+1, k_e) - Ez2(i_e-1, j_e, k_e)*Jx;
EyN(i_e, j_e, k_e) = EyN(i_e, j_e, k_e) - Ey2(i_e-1, j_e, k_e-1)*Jx;
EyN(i_e, j_e, k_e+1) = EyN(i_e, j_e, k_e+1) + Ey2(i_e-1, j_e, k_e)*Jx;

EzN(i_e+1, j_e, k_e) = EzN(i_e+1, j_e, k_e) + Ez2(i_e, j_e-1, k_e)*Jx;
EzN(i_e+1, j_e+1, k_e) = EzN(i_e+1, j_e+1, k_e) - Ez2(i_e, j_e, k_e)*Jx;
EyN(i_e+1, j_e, k_e) = EyN(i_e+1, j_e, k_e) - Ey2(i_e, j_e, k_e-1)*Jx;
EyN(i_e+1, j_e, k_e+1) = EyN(i_e+1, j_e, k_e+1) + Ey2(i_e, j_e, k_e)*Jx;
% step n
Curl1 = -1/d*(EyP(i_e, j_e, k_e+1) - EyP(i_e, j_e, k_e) + EzP(i_e, j_e, k_e)
- EzP(i_e, j_e+1, k_e));
Curl2 = -1/d*(EyP(i_e+1, j_e, k_e+1) - EyP(i_e+1, j_e, k_e) + EzP(i_e+1, j_e,
k_e) - EzP(i_e+1, j_e+1, k_e));
Curlx = 0.5*(Curl1 + Curl2);
AntEx = 1/4*(ExP(i_e, j_e, k_e)+...
ExP(i_e, j_e+1, k_e)+...
ExP(i_e, j_e, k_e+1)+...
ExP(i_e, j_e+1, k_e+1)); % E-fields for
all ports -step n
AntHx = 0.5*(HxN(i_e, j_e, k_e) + HxN(i_e+1, j_e, k_e)); % H-fields
for all ports -step n+1/2

% coil/loop along the y-axis
% Update equations (simple addition - right-hand rule exactly)
EzN(i_e, j_e, k_e) = EzN(i_e, j_e, k_e) - Ez2(i_e-1, j_e-1, k_e)*Jy;
EzN(i_e+1, j_e, k_e) = EzN(i_e+1, j_e, k_e) + Ez2(i_e, j_e-1, k_e)*Jy;
ExN(i_e, j_e, k_e) = ExN(i_e, j_e, k_e) + Ex2(i_e, j_e-1, k_e-1)*Jy;
ExN(i_e, j_e, k_e+1) = ExN(i_e, j_e, k_e+1) - Ex2(i_e, j_e-1, k_e)*Jy;
EzN(i_e, j_e+1, k_e) = EzN(i_e, j_e+1, k_e) - Ez2(i_e-1, j_e, k_e)*Jy;
EzN(i_e+1, j_e+1, k_e) = EzN(i_e+1, j_e+1, k_e) + Ez2(i_e, j_e, k_e)*Jy;
ExN(i_e, j_e+1, k_e) = ExN(i_e, j_e+1, k_e) + Ex2(i_e, j_e, k_e-1)*Jy;

```

```

ExN(i_e, j_e+1, k_e+1) = ExN(i_e, j_e+1, k_e+1) - Ex2(i_e, j_e, k_e)*Jy;
% step n
Curl1 = -1/d*(EzP(i_e+1, j_e, k_e) - EzP(i_e, j_e, k_e) + Exp(i_e, j_e, k_e) -
Exp(i_e, j_e, k_e+1));
Curl2 = -1/d*(EzP(i_e+1, j_e+1, k_e) - EzP(i_e, j_e+1, k_e) + Exp(i_e, j_e+1,
k_e) - Exp(i_e, j_e+1, k_e+1));
Curly = 0.5*(Curl1 + Curl2);
AntEy      = 1/4*(EyP(i_e, j_e, k_e)+...
                EyP(i_e+1, j_e, k_e)+...
                EyP(i_e, j_e, k_e+1)+...
                EyP(i_e+1, j_e, k_e+1));           % E-fields for
all ports -step n
AntHy      = 0.5*(HyN(i_e, j_e, k_e) + HyN(i_e, j_e+1, k_e));           % H-fields
for all ports -step n+1/2

% coil/loop along the z-axis
% Update equations (simple addition - right-hand rule exactly)
ExN(i_e, j_e, k_e)      = ExN(i_e, j_e, k_e) - Ex2(i_e, j_e-1, k_e-1)*Jz;
ExN(i_e, j_e+1, k_e)    = ExN(i_e, j_e+1, k_e) + Ex2(i_e, j_e, k_e-1)*Jz;
EyN(i_e, j_e, k_e)      = EyN(i_e, j_e, k_e) + Ey2(i_e-1, j_e, k_e-1)*Jz;
EyN(i_e+1, j_e, k_e)    = EyN(i_e+1, j_e, k_e) - Ey2(i_e, j_e, k_e-1)*Jz;
ExN(i_e, j_e, k_e+1)    = ExN(i_e, j_e, k_e+1) - Ex2(i_e, j_e-1, k_e)*Jz;
ExN(i_e, j_e+1, k_e+1)  = ExN(i_e, j_e+1, k_e+1) + Ex2(i_e, j_e, k_e)*Jz;
EyN(i_e, j_e, k_e+1)    = EyN(i_e, j_e, k_e+1) + Ey2(i_e-1, j_e, k_e)*Jz;
EyN(i_e+1, j_e, k_e+1)  = EyN(i_e+1, j_e, k_e+1) - Ey2(i_e, j_e, k_e)*Jz;

% step n
Curl1 = -1/d*(Exp(i_e, j_e+1, k_e) - Exp(i_e, j_e, k_e) + EyP(i_e, j_e, k_e) -
EyP(i_e+1, j_e, k_e));
Curl2 = -1/d*(Exp(i_e, j_e+1, k_e+1) - Exp(i_e, j_e, k_e+1) + EyP(i_e, j_e, k_e+1)
- EyP(i_e+1, j_e, k_e+1));
Curlz = 0.5*(Curl1 + Curl2);

AntEz      = 1/4*(EzP(i_e, j_e, k_e)+...
                EzP(i_e+1, j_e, k_e)+...
                EzP(i_e, j_e+1, k_e)+...
                EzP(i_e+1, j_e+1, k_e));           % E-fields
for all ports -step n
AntHz      = 0.5*(HzN(i_e, j_e, k_e)+HzN(i_e, j_e, k_e+1));           % H-fields
for all ports -step n+1/2

% co-polar components
AntE(m, kt) = PortNX(m) *AntEx + PortNY(m) *AntEy + PortNZ(m) *AntEz;           % at step
n - tested

```

```

TmpH(m, kt) = PortNX(m)*Anthx + PortNY(m)*AntHy + PortNZ(m)*AntHz;      % at step
n+1/2 - tested
Anth(m, kt) = (TmpH(m, kt) + TmpH(m, kt-1))/2;                          % at step
n - tested
AntI(m, kt) = IG(m, kt);
Curl      = PortNX(m)*Curlx + PortNY(m)*Curly + PortNZ(m)*Curlz;
AntV(m, kt) = PortM(m)*Curl;      % antenna voltages for all ports
at step n
AntV(m, kt) = -mu0*PortM(m)*(TmpH(m, kt) - TmpH(m, kt-1))/dt;

```

Same as the electrical dipole case, the advantage here is the ability to describe the coil of arbitrary orientation as well, whilst keeping the same phase center. Its disadvantage is also a “large” volume occupied by the coil model that extends to two unit cells in every direction. The above coil model may be treated as a symmetric point source model.

3.2.4. Mutual inductance between transmit and receive coils

Although not directly implemented in the code, the mutual inductance between transmit and receive coils as a function of frequency can be calculated after the FDTD run is finished. The result has the form

$$L_{ml}(\omega) = \frac{\text{fft}(E_{emf}^m(t))}{j\omega \text{fft}(i^1(t))} = -\mu_0 AN \frac{\text{fft}(H_{x,y,z}^m(t))}{\text{fft}(i^1(t))} \quad (3-26)$$

Note that the current is to be given on the half temporal grid – see Eqs. (3-22) – whereas the emf voltage is found on the integer temporal grid – see Eq. (3-10b). Therefore, for example, one could interpolate the current for the integer temporal grid.

3.3 Model of an impressed electric field or voltage source (loop of magnetic current)

3.3.1. Concept of an impressed voltage (electric field) source

Considered two metal plates of area A separated by distance l in Fig. 3-6 with an applied voltage $v(t)$ between the plates. Assume that the corresponding electric field (directed down in Fig. 3-6),

$$E_{in}(t) = \frac{v(t)}{l} \quad (3-27)$$

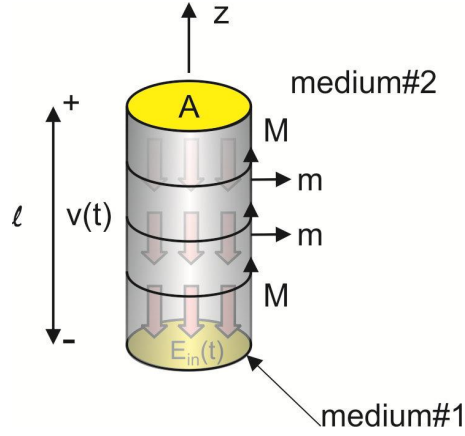


Figure 3-6 Impressed voltage (electric field source)

is uniform between the plates, which is true for small separation distances. Also assume that the electric field is zero otherwise (medium#2). The boundary condition for the electric field on the side boundary of the cylinder states that

$$\vec{M} = -\vec{m} \times (\vec{E}_2 - \vec{E}_{in}(t)) \quad (3-28)$$

where \vec{M} is the resulting surface magnetic current density (V/m) on the side boundary, \vec{m} is the outer normal. With reference to Fig. 2-1, \vec{M} has only an angular component, i.e.

$$M_\phi = E_{in}(t) = \frac{v(t)}{l} \quad (3-29a)$$

Thus, the impressed electric field source (or the voltage source) is equivalent to the loop of a surface magnetic current. The total magnetic current in the loop is lM_ϕ , the loop area is A. Therefore, the product $AlM_\phi = Av(t)$ has the sense of a loop moment where A is the moment per one volt.

3.3.2. Modeling an impressed voltage source

The initial FDTD implementation is shown in Fig. 3-7. The field source from Fig. 2-1 is placed at the node of the co-polar electric field as shown in Fig. 3-7. Such a location is convenient, but it does not allow us to consider an arbitrary source orientation in general. We model the source with the closed loop of a magnetic

current $i_{ms}(t)$ passing through the nodes for the magnetic field shown in the figure. This model is dual to the magnetic dipole. Since the loop moment should be preserved, it follows from Eq. (3-29a) that

$$i_{ms}(t) = \frac{A}{\Delta^2} v(t) \quad (3-29b)$$

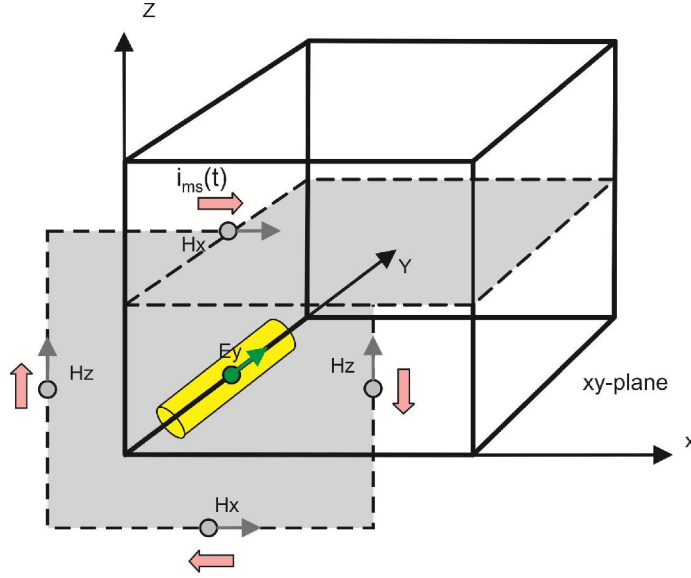


Figure 3-7 TX voltage source and the surrounding FDTD grid

Thus, the volumetric magnetic current density, $J_{ms}(t) = i_{ms}(t)/\Delta^2$, in Fig. 3-7 is specified. The update equations corresponding to Fig. 3-7 have the form

$$H_x^{n+1/2}(i, j, k) = H_{x1} H_x^{n-1/2}(i, j, k) + H_{x2} \times (E_n^y(i, j, k+1) - E_n^y(i, j, k) + E_n^z(i, j, k) - E_n^z(i, j+1, k) - \Delta J_{ms}^n) \quad (3-30a)$$

$$H_x^{n+1/2}(i, j, k-1) = H_{x1} H_x^{n-1/2}(i, j, k-1) + H_{x2} \times (E_n^y(i, j, k) - E_n^y(i, j, k-1) + E_n^z(i, j, k-1) - E_n^z(i, j+1, k-1) + \Delta J_{ms}^n) \quad (3-30b)$$

$$H_z^{n+1/2}(i, j, k) = H_{z1} H_z^{n-1/2}(i, j, k) + H_{z2} \times (E_x^n(i, j+1, k) - E_x^n(i, j, k) + E_y^n(i, j, k) - E_y^n(i+1, j, k) + \Delta J_{ms}^n) \quad (3-30c)$$

$$H_z^{n+1/2}(i-1, j, k) = H_{z1} H_z^{n-1/2}(i-1, j, k) + H_{z2} \times (E_x^n(i-1, j+1, k) - E_x^n(i-1, j, k) + E_y^n(i-1, j, k) - E_y^n(i, j, k) - \Delta J_{ms}^n) \quad (3-30d)$$

An important observation is that it is very straightforward to implement Eqs. (3-30) in practice. Namely, only current excitation terms have to be added after the standard update equations for the magnetic field.

3.3.3. Modeling an impressed voltage source with Coincident Phase Centers

The magnetic current-loop model of Fig. 3-7 is straightforwardly modified for the case of arbitrary source orientation. The concept is shown in Fig. 3-8 that follows. The source antenna is now placed at the corner of the Yee cell. The source in Fig. 3-8 is replaced by two square loops of the grid-aligned magnetic current, which in sum possess the same moment. This means that the current density for each loop becomes the half of the original magnetic current density.

Update Eqs. (3-30) are straightforwardly modified to the present case: they remain the same for the upper face in Fig. 3-8 and employ the index substitution $j \rightarrow j - 1$ for the lower face.

The source of arbitrary orientation with the unit direction vector \vec{n} is considered as a superposition of three elementary sources directed along the x-, y-, and z-axes. The corresponding current densities are given by

$$J_{msX}(t) = \frac{1}{2} n_x J_{ms}(t), \quad J_{msY}(t) = \frac{1}{2} n_y J_{ms}(t), \quad J_{msZ}(t) = \frac{1}{2} n_z J_{ms}(t) \quad (3-31)$$

All the magnetic current densities should follow the right-hand rule with regard to all three Cartesian axes as shown in Fig. 3-8 for the y-axis.

This case has the same properties as the two cases before. A “large” volume impressed voltage occupied by the dipole model that extends to two unit cells in every direction, while able to describe the source of arbitrary orientation with same phase center.

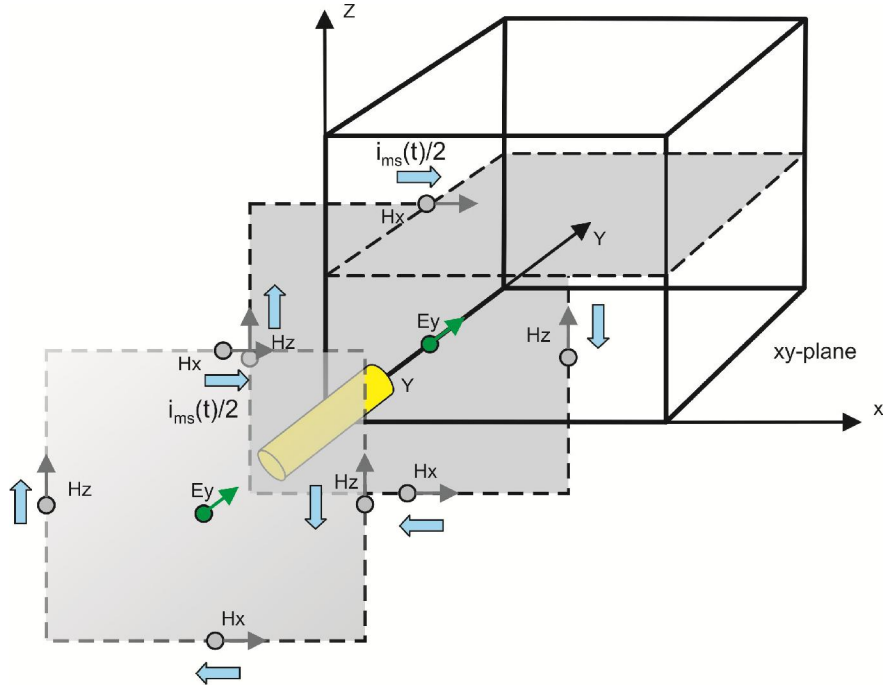


Figure 3-8 Impressed source model with the dipole placed at the corner node of the Yee cell

3.3.4. Relation between the magnetic current loop source and the electric dipole source

The displacement current (current in the capacitor) in Fig. 3-6 is directed down. Therefore, the counterpart of the magnetic current loop in Fig. 3-6, with the magnetic current running following the right-hand rule with regard to the positive z-direction, should be an infinitesimally small electric dipole oriented toward the negative z-direction. If this dipole has a length l and driven by current $i_s(t) = I_{0s} \cos \omega t$, its radiation in the far field is described below [22]

$$\begin{aligned}
 E_{\theta} &= -j \frac{\eta k I_{0s} l}{4\pi r} \sin \theta \exp(-jkr) \\
 H_{\phi} &= -j \frac{k I_{0s} l}{4\pi r} \sin \theta \exp(-jkr)
 \end{aligned}
 \tag{3-32}$$

On the other hand, the small magnetic current loop, whose right-hand rule axis is the z-axis, and which has a uniform magnetic current $i_{ms}(t) = I_{0ms} \cos \omega t$ and an area S , radiates in the far field in the following way:

$$\begin{aligned}
E_{\theta} &= \frac{k^2 I_{0ms} S}{4\pi r} \sin \theta \exp(-jkr) \\
H_{\phi} &= \frac{k^2 I_{0ms} S}{\eta 4\pi r} \sin \theta \exp(-jkr)
\end{aligned} \tag{3-33}$$

Comparing Eqs.(3-32) and (3-33) one has

$$k^2 I_{0ms} S = -j\eta k I_{0s} l \Rightarrow I_{0s} = jk \frac{S}{l\eta} I_{0m} \tag{3-34}$$

Eq. (3-34) can be transformed to the time-domain solution for an arbitrary pulse by operator substitution $jk \rightarrow c_0^{-1} \partial/\partial t$. This gives

$$i_s(t) = \varepsilon \frac{S}{l} \frac{\partial i_{ms}(t)}{\partial t} \Rightarrow i_{ms}(t) = \frac{l}{\varepsilon S} \int_0^t i_s(t') dt' \tag{3-35}$$

Further, the magnetic current $i_{ms}(t)$ is replaced by its current density uniformly distributed over every involved cell's cross-section:

$$J_{ms}(t) = \frac{i_{ms}(t)}{\Delta^2} = \frac{l}{\Delta^2 \varepsilon S} \int_0^t i_s(t') dt' \tag{3-36}$$

Finally, since the loop area is the cell face, one has

$$J_{ms}(t) = \frac{l}{\Delta^4 \varepsilon} \int_0^t i_s(t') dt' \tag{3-37}$$

The above expression has the units of V/m², indeed. The last step is to substitute into Eq. (3-37) the expression for $J_{ms}(t)$ that follows from Eq. (3-29b), that is

$$J_{ms}(t) = \frac{A v(t)}{\Delta^4} \tag{3-38}$$

The result becomes

$$i_s(t) = C \frac{dv}{dt}, \quad C = \frac{\epsilon A}{l} \quad (3-39)$$

which is the familiar capacitor model introduced yet in the first figure to this section.

3.4 Performance validation

A couple test benchmarks will be shown below to verify the performance of the CPCs model and traditional point source model.

An electrical dipole, a magnetic dipole and an impressed voltage source described in previous sections will be investigated as different cases — see Table 3-1.

Table 3-1 CARTESIAN CURRENT DENSITY COMPONENTS

Source Type	Current Density ($\mathbf{i} = \mathbf{x}, \mathbf{y}, \mathbf{z}$)	Relevant Parameters
Electric Dipole	$J_{si}(t) = \frac{1}{2} n_i J_s(t)$	$J_s(t)$: current density of original dipole
Magnetic Dipole	$J_{si}(t) = \frac{1}{2} n_i \frac{AN}{\Delta^4} i(t)$	$i(t)$: coil current A : coil area N : number of turns
Impressed Voltage Source	$J_{msi}(t) = \frac{1}{2} n_i J_{ms}(t)$	$J_{ms}(t)$: magnetic current density of arbitrarily-oriented loop of magnetic current

3.4.1 Pulse form to be used

To start the simulation, a specific source should be assigned. In general, the pulse form may be chosen arbitrarily. A bipolar Gaussian (Rayleigh) current pulse used in the following test benchmarks has the form.

$$i_s(t) = I_0 \frac{(t_0 - t)}{\tau} \exp\left(\frac{-(t - t_0)^2}{(2\tau)^2}\right), \quad t_0 = 5\tau \quad (3-40)$$

Its center frequency and a 3dB-power bandwidth are given by

$$f_c = \frac{0.16}{\tau}, \quad \text{BW} = 1.15 f_c \quad (3-41)$$

$$\text{Here, } \tau = 0.2 \text{ ns}; \Rightarrow f_c = 800 \text{ MHz} \quad (3-42)$$

3.4.2 Transmit (TX) Electrical dipole case

In this case, a transmit (TX) electrical dipole is considered, the parameters can be found in Table 3-2

Table 3-2 Test parameters

Domain size	Cell size	Pulse center frequency/wavelength	Cells per wavelength at center frequency
1.2×1.2×1.2m	20mm or 10mm	800MHz $\lambda = 375\text{mm}$	18.75 or 37.5
Excitation port	Receiver/probe ports		
One dipole centered at origin and oriented along the z-axis with the electric moment 10^{-3} m per one ampere	Three field probes at the distances 60, 200, and 340mm oriented along the z-axis to sample the radiated vertical electric field in the E-plane (the xz-plane)		

The results are shown below in Fig 3-9. Port #1 indicates the transmit dipole, Ports #2 ~ #4 indicate the field probes at distances 60, 200, and 340mm respectively.

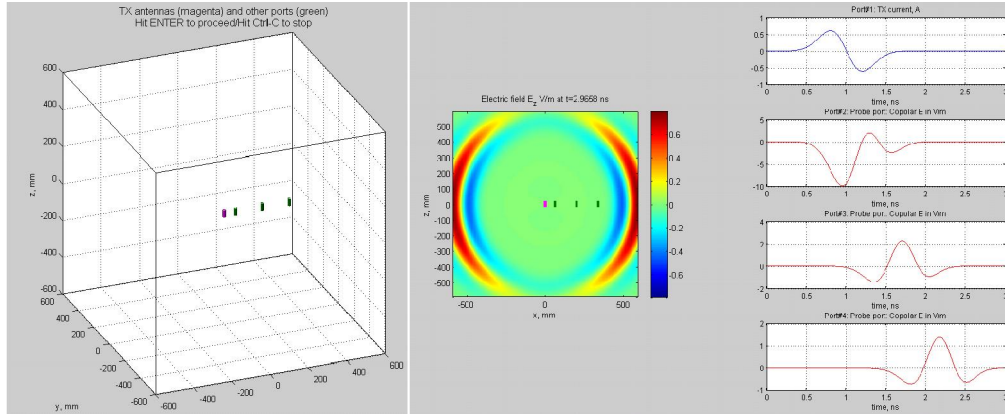


Figure 3-9 a) Test geometry and b) Test output

For harmonic excitation, the vertical E-field component of an infinitesimally-small electric dipole of length l in the xz-plane at $z = 0$ is given in the phasor form [22] by

$$E_z(y, z = 0) = -E_\theta(y, z = 0) = -\eta \left[\frac{1}{r} + jk + \frac{1}{jkr^2} \right] \frac{M_{z0}}{4\pi r} \exp(-jkr) \quad (3-43)$$

where $M_{z0} = Il_0$ is the corresponding dipole moment. Eq. (3-43) can be transformed

to the time-domain solution for an arbitrary pulse by operator substitution $jk \rightarrow c_0^{-1} \partial/\partial t$. This yields, in time domain

$$E_z(y, z = 0) = \frac{-\eta}{4\pi r} \left[\frac{M_z(t-r/c_0)}{r} + \frac{1}{c_0} \frac{\partial M_z(t-r/c_0)}{\partial t} + \frac{c_0 \int_0^{t-r/c_0} M_z(t') dt'}{r^2} \right] \quad (3-44)$$

where now

$$M_z(t) = li(t) \quad (3-45)$$

is the instantaneous dipole moment of the small dipole with $i(t)$ being the instantaneous dipole current in amperes given by Eq. (1) of the introduction. One can see that the transmitted electric field is a combination of the dipole current, of its first derivative, and of its integral. The first derivative dominates in the far field.

Fig. 3-10a shows the comparison results between two pulse forms (red-FDTD, blue-analytical) for three probes. The agreement is good for the closest probe, but it becomes slightly worse when the probe is moved from the near field into the Fresnel region. Note that the closest probe is located at the distance of three unit cells (0.16λ) from the antenna.

Fig. 3-10b shows the same results, but when the cell size in this example is reduced to 10mm.

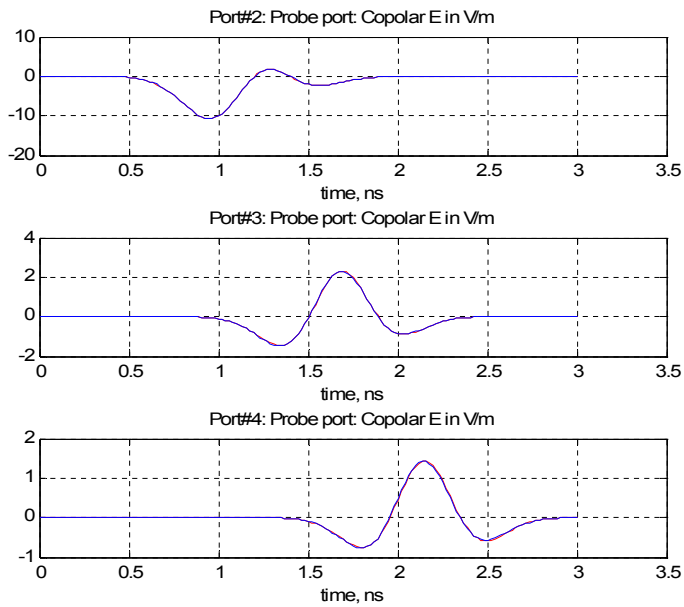
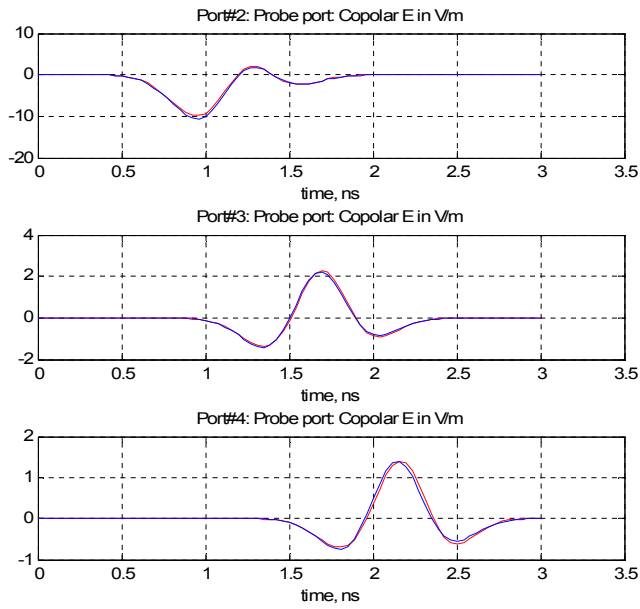


Figure 3-10 Comparison results for a)20mm and b)10mm cell size. Blue – exact analytical solution; red – FDTD.

3.4.3 Arbitrarily oriented Electric TX dipole(s)

In this case, a 45 degree rotated TX electrical dipole and a non-grid aligned receive probe are considered. The detail parameters can be found in Table 3-3

Table 3-3 Test parameters

Domain Size	Cell size	Pulse center frequency/wavelength	Cells per wavelength at center frequency
1.2×1.2×1.2m	20mm or 10mm	800MHz $\lambda = 375\text{mm}$	18.75 or 37.5
Excitation port	Receiver/probe ports		
One dipole centered at origin and located in the xz-plane at 45° elevation angle with the electric moment 10^{-3} m per one ampere	Two field probes located at (60,0,0)mm and (200,0,200)mm, respectively. The first probe is along the z-axis, the second probe is located in the xz-plane at 45° elevation angle		

The results are shown below in Fig 3-11. Port #1 indicates the transmit dipole, Port #2 indicates the field probes at distances 60mm, and Port #3 indicates the non-grid aligned probe at (200,0,200)mm.

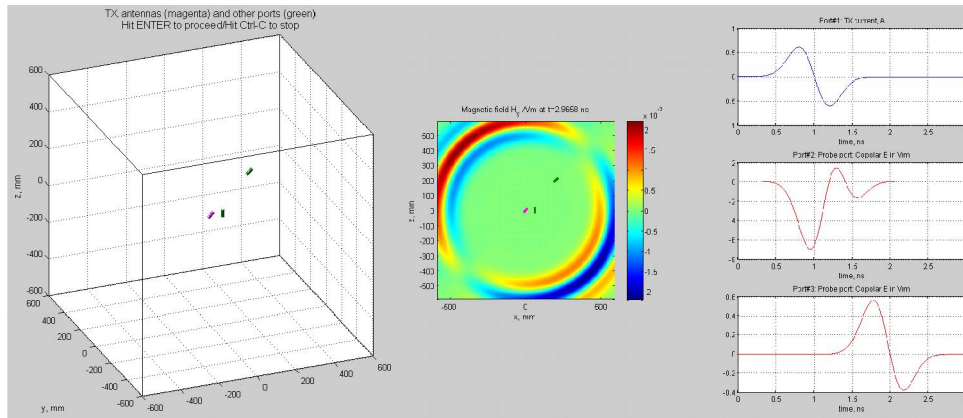


Figure 3-11 a) Test geometry and b) Test output

For this problem both E -field components of an infinitesimally-small dipole of length l will be needed. For the small dipole oriented along the z -axis [22]

$$E_{\theta} = \eta \sin \theta \left[\frac{1}{r} + jk + \frac{1}{jkr^2} \right] \frac{M_{z0}}{4\pi r} \exp(-jkr), \quad E_r = \eta \cos \theta \left[\frac{2}{r} + \frac{2}{jkr^2} \right] \frac{M_{z0}}{4\pi r} \exp(-jkr) \quad (3-46)$$

where $M_{z0} = Il_0$ is the corresponding dipole moment. Eq. (3-46) can be transformed to the time-domain solution for an arbitrary pulse by operator substitution $jk \rightarrow c_0^{-1} \partial/\partial t$. This yields, in time domain

$$\begin{aligned}
E_{\theta} &= \frac{\eta \sin \theta}{4\pi r} \left[\frac{M_z(t-r/c_0)}{r} + \frac{1}{c_0} \frac{\partial M_z(t-r/c_0)}{\partial t} + \frac{c_0 \int_0^{t-r/c_0} M_z(t') dt'}{r^2} \right] \\
E_r &= \frac{\eta \cos \theta}{4\pi r} \left[\frac{2M_z(t-r/c_0)}{r} + \frac{2c_0 \int_0^{t-r/c_0} M_z(t') dt'}{r^2} \right]
\end{aligned} \tag{3-47}$$

where now

$$M_z(t) = li(t) \tag{3-48}$$

is the instantaneous dipole moment of the small dipole with $i(t)$ being the instantaneous dipole current in amperes given by Eq. (3-46) of the introduction.

The first probe (port#2) acquires the field $E_1(t, r) = -E_{\theta}(45^{\circ}, t, r = 60 \text{ mm})$.

The second probe (port#3) acquires the field $E_2(t, r) = +E_r(0^{\circ}, t, r = \sqrt{2} \times 200 \text{ mm})$.

These fields are to be compared with the numerical solution.

Fig. 3-12a shows the comparison results between two pulse forms (red-FDTD, blue-analytical) for three probes. The agreement is good for both probes, but not nearly perfect. Note that the closest probe is located at the distance of three unit cells (0.16λ) from the antenna center.

Fig. 3-12b shows the same results, but when the cell size in this example is reduced to 10mm. All other parameters remain the same. The agreement is now excellent. For example, the difference between analytical and numerical solutions in the bottom plot of Fig. 3-12b can hardly be recognized visually.

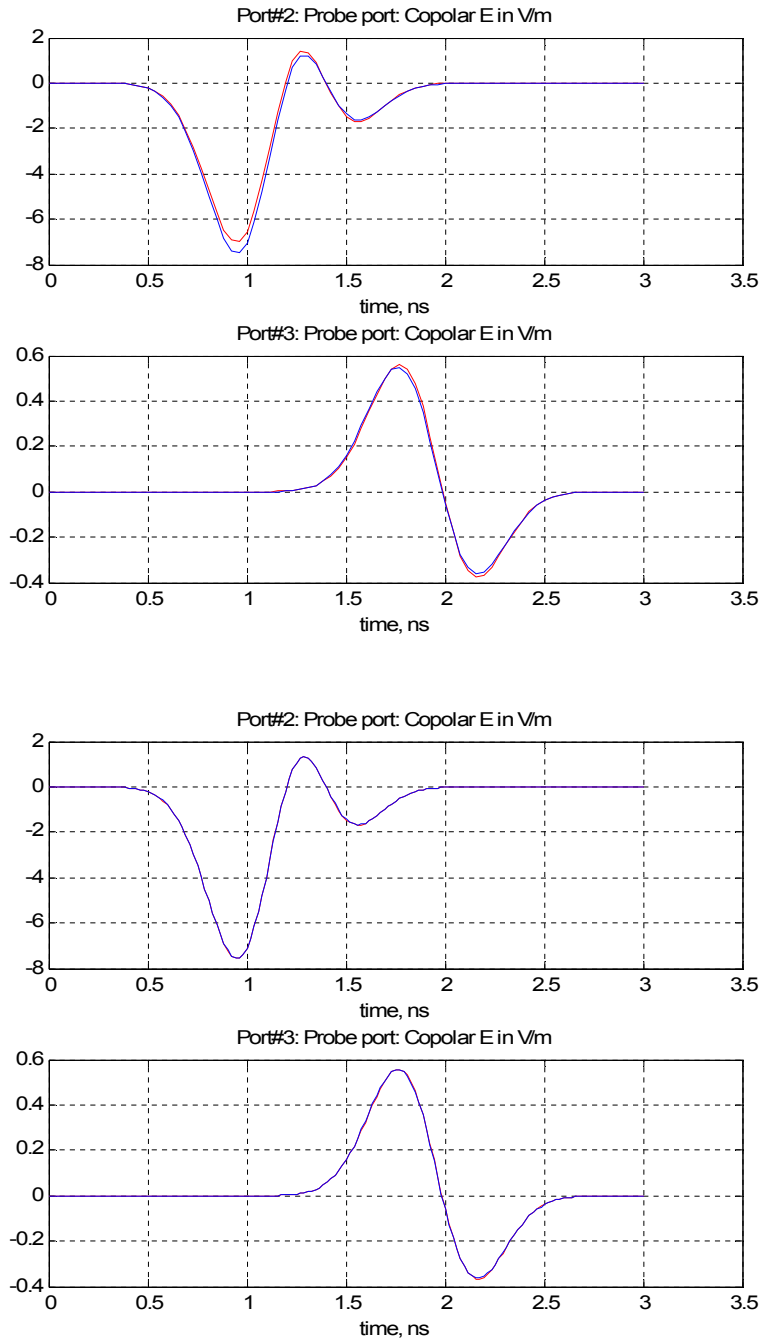


Figure 3-12 Comparison results for a) 20mm and b) 10mm cell size. Blue – exact analytical solution; red – FDTD.

3.4.4 TX coil in free space

In this case, a TX magnetic dipole (coil) is investigated. The detail parameters can be found in Table 3-4.

Table 3-4 Test parameters

Domain Size	Cell size	Pulse center frequency/wavelength	Cells per wavelength at center frequency
1.2×1.2×1.2m	20mm or 10mm	800MHz $\lambda = 375\text{mm}$	18.75 or 37.5
Excitation port	Receiver/probe ports		
One coil centered at origin and oriented along the z-axis with the magnetic moment 10^{-3} m^2 per one ampere	Three field probes at the distances 100, 200, and 300mm oriented along the y-axis to sample the radiated azimuthal electric field in the E-plane (the xy-plane)		

The results are shown below in Fig 3-13. Port #1 indicates the transmit coil, Ports #2~#4 indicate the field probes at the distances 100, 200, and 300mm oriented along the y-axis.

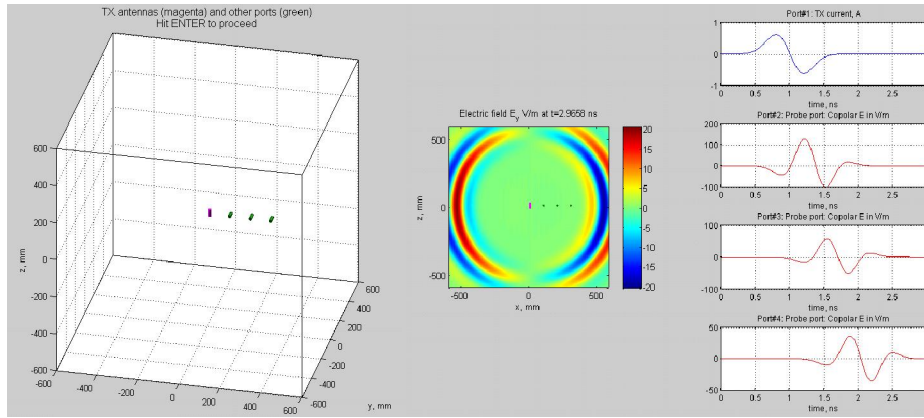


Figure 3-13 a) Test geometry and b) Test output

For harmonic excitation, the radiating E -field component in the xy -plane at $x > 0$ is given in the phasor form by [22]

$$E_y(y=0, z=0) = E_\phi(y=0, z=0) = \eta \left[k^2 + \frac{k}{jr} \right] \frac{M_{z0}}{4\pi r} \exp(-jkr) \quad (3-49)$$

where $M_{z0} = ANI_0$ is the corresponding magnetic moment. Eq. (3-49) can be transformed to the time-domain solution for an arbitrary pulse by operator substitution $jk \rightarrow c_0^{-1} \partial/\partial t$. This yields, in time domain

$$E_y(y=0, z=0) = E_\phi(y=0, z=0) = -\eta \left[\frac{1}{c_0^2} \frac{\partial^2 M_z(t-r/c_0)}{\partial t^2} + \frac{1}{c_0 r} \frac{\partial M_z(t-r/c_0)}{\partial t} \right] \frac{1}{4\pi r}$$

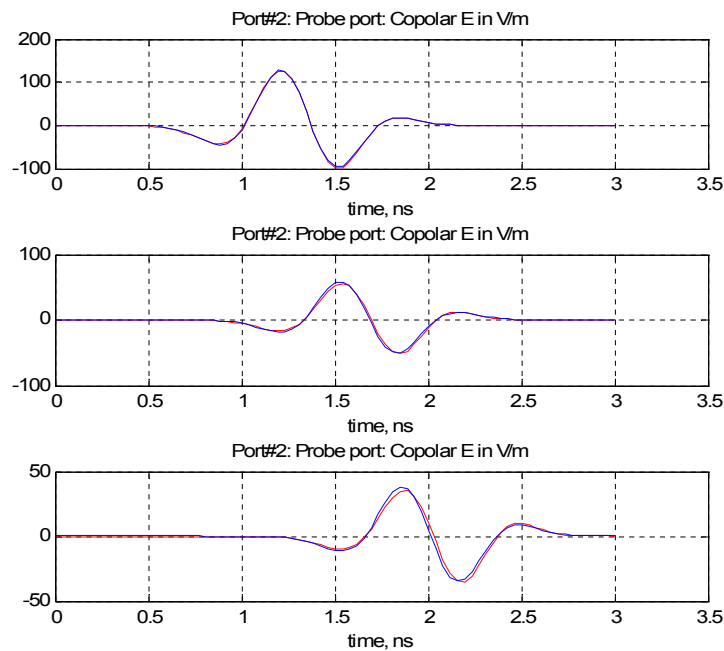
(3-50)

where now

$$M_z(t) = ANi(t) \tag{3-51}$$

is the instantaneous magnetic moment of the coil with $i(t)$ being the instantaneous coil current in amperes given by Eq. (3-49) of the introduction. One can see that the transmitted electric field is a combination of the first and second derivatives of the coil current; the second derivative dominates in the far field.

Fig. 3-14a shows the comparison results between two pulse forms (red-FDTD, blue-analytical) for three probes. The agreement is good, but it becomes slightly worse when the probe is moved from the near field into the Fresnel region. Fig. 3-14b shows the same results, but when the cell size in this example is reduced to 10mm. All other parameters remain the same. The agreement is now excellent.



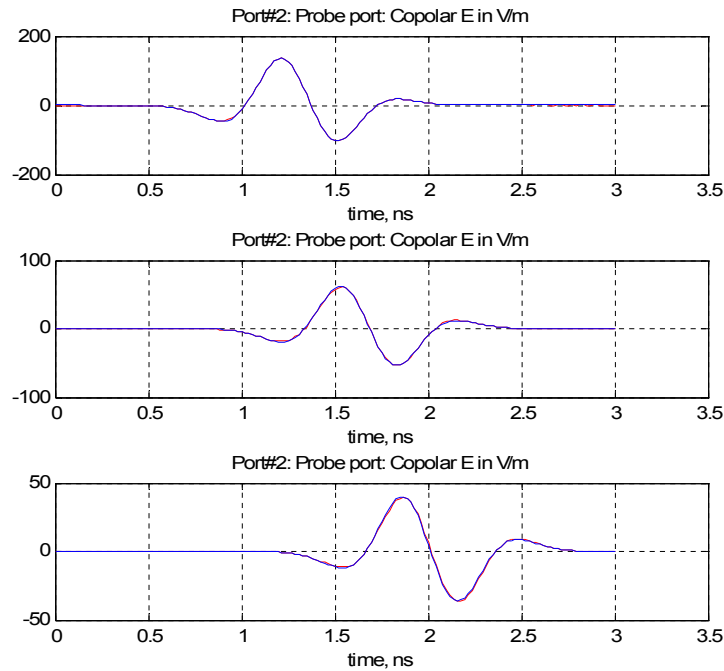


Figure 3-14 Comparison results for a) 20mm and b) 10mm cell size. Blue – exact analytical solution; red – FDTD.

3.4.5 TX and RX coils in free space

Compared to previous case, the receive probes have been replaced by coils located at the distances 60 and 320mm, respectively oriented along the z-axis to generate the open-circuit voltage. The detail parameters can be found in Table 3-5

Table 3-5 Test parameters

Domain Size	Cell size	Pulse center frequency/wavelength	Cells per wavelength at center frequency
1.2×1.2×1.2m	20mm or 10mm	800MHz $\lambda = 375\text{mm}$	18.75 or 37.5
Excitation port	Receiver/probe ports		
One TX coil centered at origin and oriented along the z-axis with the magnetic moment 10^{-3} m^2 per one ampere	Two receiver (RX) coils at the distances 60 and 320mm, respectively oriented along the z-axis to generate the open-circuit voltage, with the same magnetic moment		

Graphic results can be found below in Fig 3-15. Port #1 indicates the transmit coil,

Ports #2~#3 indicate the receive coils.

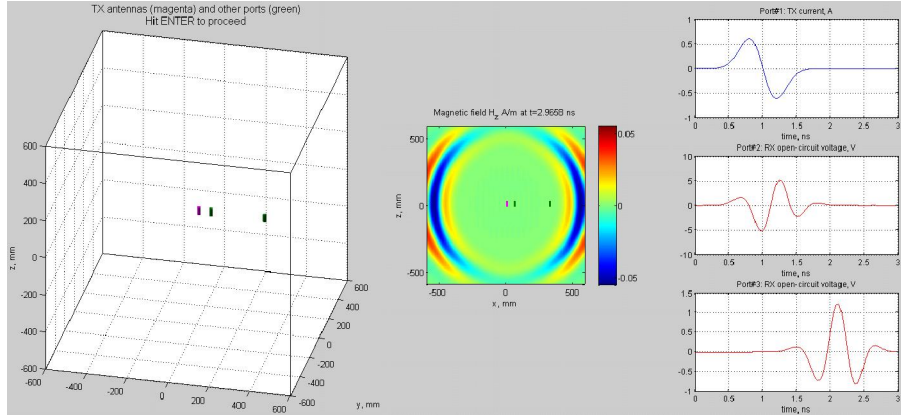


Figure 3-15 a) Test geometry and b) Test output

For harmonic excitation, the radiating H -field component in the xy -plane at $x > 0$ is given in the phasor form [22] by

$$H_z(y=0, z=0) = -H_\theta(y=0, z=0) = \left[k^2 + \frac{k}{jr} - \frac{1}{r^2} \right] \frac{M_{z0}}{4\pi r} \exp(-jkr) \quad (3-52)$$

where $M_{z0} = ANI_0$ is the corresponding magnetic moment. Eq. (3-52) can be transformed to the time-domain solution for an arbitrary pulse by operator substitution $jk \rightarrow c_0^{-1} \partial/\partial t$. This yields, in time domain

$$H_z(y=0, z=0) = -H_\theta(y=0, z=0) = - \left[\frac{1}{c_0^2} \frac{\partial^2 M_z(t-r/c_0)}{\partial t^2} + \frac{1}{c_0 r} \frac{\partial M_z(t-r/c_0)}{\partial t} + \frac{1}{r^2} M_z(t-r/c_0) \right] \frac{1}{4\pi r} \quad (3-53)$$

where now

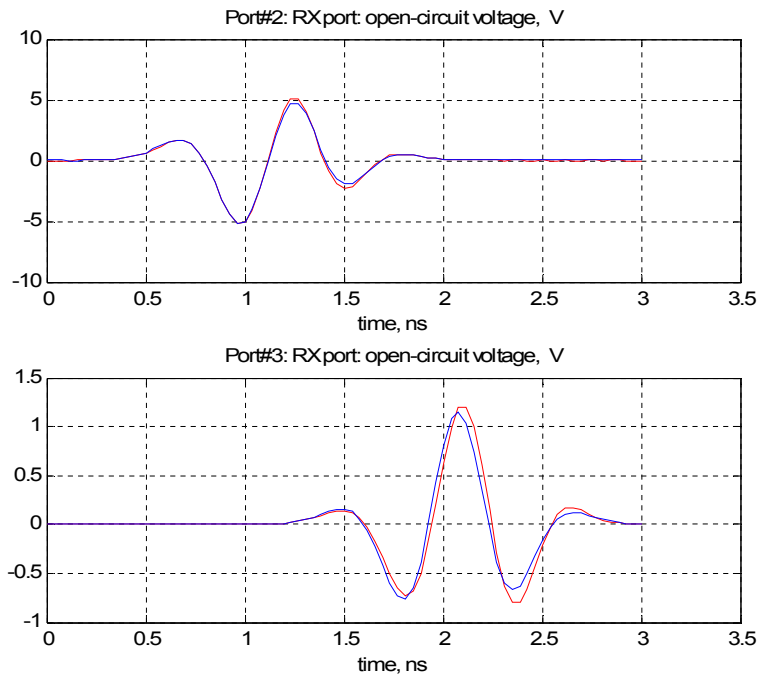
$$M_z(t) = ANi(t) \quad (3-54)$$

is the instantaneous magnetic moment of the coil with $i(t)$ being the instantaneous coil current in amperes given by Eq. (3-52) of the introduction. One can see that the transmitted magnetic field is a combination of the coil current and the first and second derivatives of the coil current; the second derivative dominates in the far field. In the receiving mode, the open-circuited air-core RX coil generates the induced emf voltage,

$$E_{emf}(t) = -\mu_0 AN \frac{\partial H_z}{\partial t} \quad (3-55)$$

Fig. 3-16a shows the comparison results between two pulse voltage forms (red-FDTD, blue-analytical) for three probes. The agreement is good in the near field, at the distance of 60 mm from the TX coil center, which corresponds to 0.16λ . However, it becomes slightly worse when the probe is moved from the near field into the Fresnel region, to the distance of 300mm.

Fig. 3-16b shows the same results, but when the cell size in this example is reduced to 10mm with all other parameters remain the same. The agreement is now very good. This result is remarkable since the third derivative of the initial current pulse is actually employed.



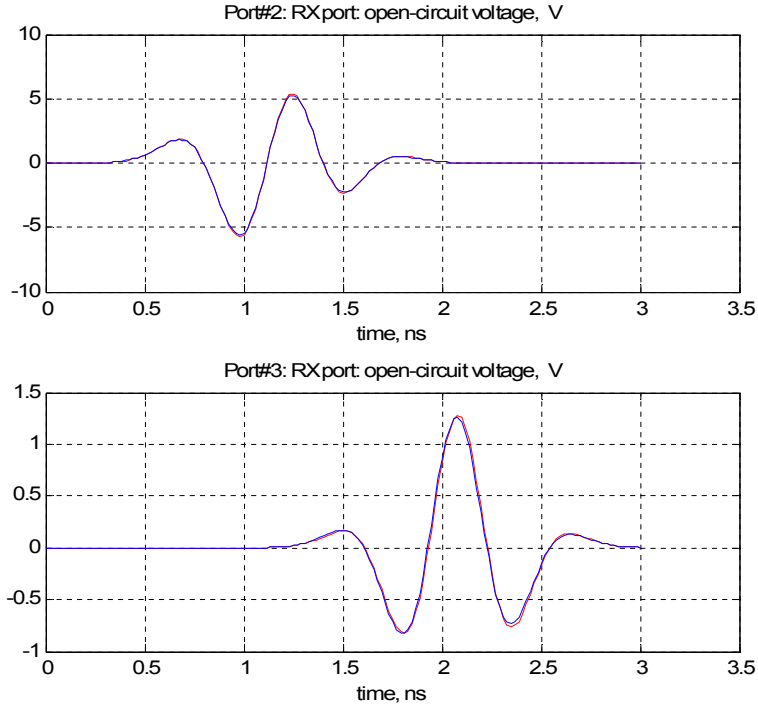


Figure 3-16 Comparison results for a) 20mm and b) 10mm cell size. Blue – exact analytical solution; red – FDTD.

3.4.6 Arbitrarily oriented TX and RX coils in free space

A test case for arbitrary oriented coils is defined using two receiver (RX) coils at the distances $x=60\text{mm}$, $z=60\text{mm}$ and $x=260\text{mm}$, $z=260\text{mm}$ from the origin, respectively. The detail parameters can be found in Table 3-6

Table 3-6 Test parameters

Domain Size	Cell size	Pulse center frequency/wavelength	Cells per wavelength at center frequency
1.2×1.2×1.2m	20mm or 10mm	800MHz $\lambda = 375\text{mm}$	18.75 or 37.5
Excitation port	Receiver/probe ports		
One TX coil centered at origin and oriented along the z-axis with the magnetic moment 10^{-3}m^2 per one ampere	Two receiver (RX) coils at the distances $x=60\text{mm}$, $z=60\text{mm}$ and $x=260\text{mm}$, $z=260\text{mm}$ from the origin, respectively, both are in the xz-plane; both coils generate the open-circuit voltage. The magnetic moment is 10^{-3}m^2 per one ampere for every coil		

The graphic results are shown below in Fig. 3-17 where Port #1 indicates the transmit coil, Ports #2~#3 indicate the receive coils at the distances $x=60\text{mm}$, $z=60\text{mm}$ and

$x=260\text{mm}$, $z=260\text{mm}$ from the origin, respectively.

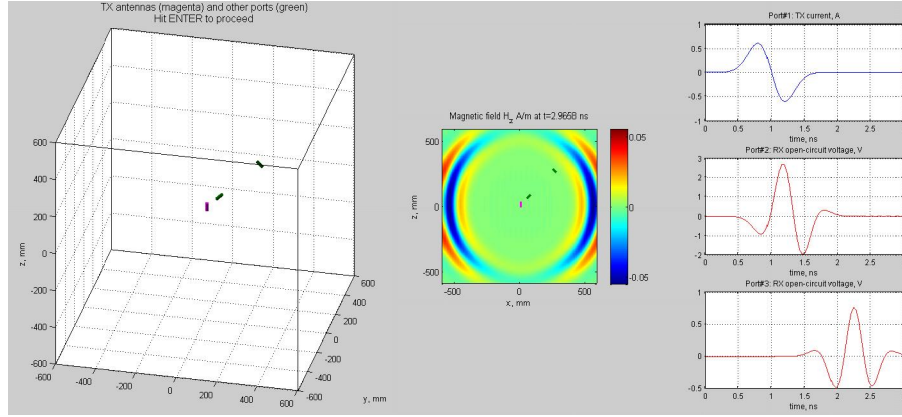


Figure 3-17 a) Test geometry and b) Test output

For harmonic excitation, the radiating H -field component at arbitrary location in the xz -plane at $x > 0$ is given in the phasor form [22] by

$$H_{\theta}(y=0) = -\sin \theta \left[k^2 + \frac{k}{jr} - \frac{1}{r^2} \right] \frac{M_{z0}}{4\pi r} \exp(-jkr) \quad (3-56)$$

where $M_{z0} = ANI_0$ is the corresponding magnetic moment. Eq. (1) can be transformed to the time-domain solution for an arbitrary pulse by operator substitution $jk \rightarrow c_0^{-1} \partial/\partial t$. This yields, in time domain

$$H_{\theta}(y=0) = \sin \theta \left[\frac{1}{c_0^2} \frac{\partial^2 M_z(t-r/c_0)}{\partial t^2} + \frac{1}{c_0 r} \frac{\partial M_z(t-r/c_0)}{\partial t} + \frac{1}{r^2} M_z(t-r/c_0) \right] \frac{1}{4\pi r} \quad (3-57)$$

where now

$$M_z(t) = ANi(t) \quad (3-58)$$

is the instantaneous magnetic moment of the coil with $i(t)$ being the instantaneous coil current in amperes given by Eq. (3-56) of the introduction. The non-radiating (radial) H -field component is given [22] by

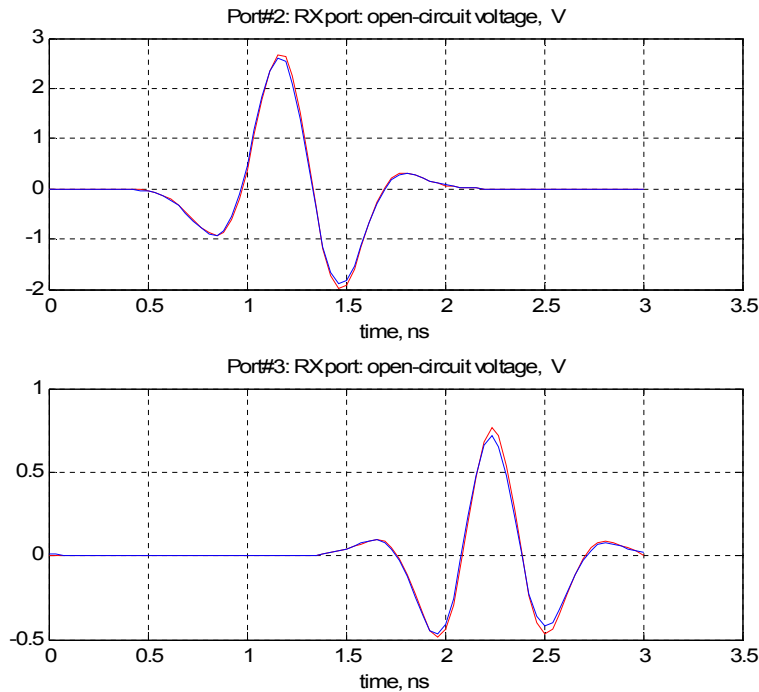
$$H_r(y=0) = \cos \theta \left[\frac{2}{rc_0} \frac{\partial M_z(t-r/c_0)}{\partial t} + \frac{2}{r^2} M_z(t-r/c_0) \right] \frac{1}{4\pi r} \quad (3-59)$$

The first (closest) receiving coil only picks up the radial component given by Eq. (3-59) at $\theta=45$ deg; the second coil only picks up the elevation component given by Eq. (3-60), also at $\theta=45$ deg. In the receiving mode, every open-circuited air-core RX coil generates the induced emf voltage,

$$E_{emf}(t) = -\mu_0 AN \frac{\partial H_z}{\partial t} \quad (3-60)$$

Fig. 3-18a shows the comparison results between two pulse voltage forms (red-FDTD, blue-analytical) for three probes. The agreement is generally good including the near field, at the radial distance of 85 mm from the TX coil center, which corresponds to 0.22λ . However, a small temporal shift of the numerical waveform appears, which is almost exactly $\Delta t/2$. It is believed that such shift appears due to the rounding procedure.

To confirm this conclusion, Fig. 3-18b shows the same results, but when the cell size in this example is reduced to 10mm. All other parameters remain the same. The agreement is now excellent. It is actually even better than for the collinear coils in the previous example.



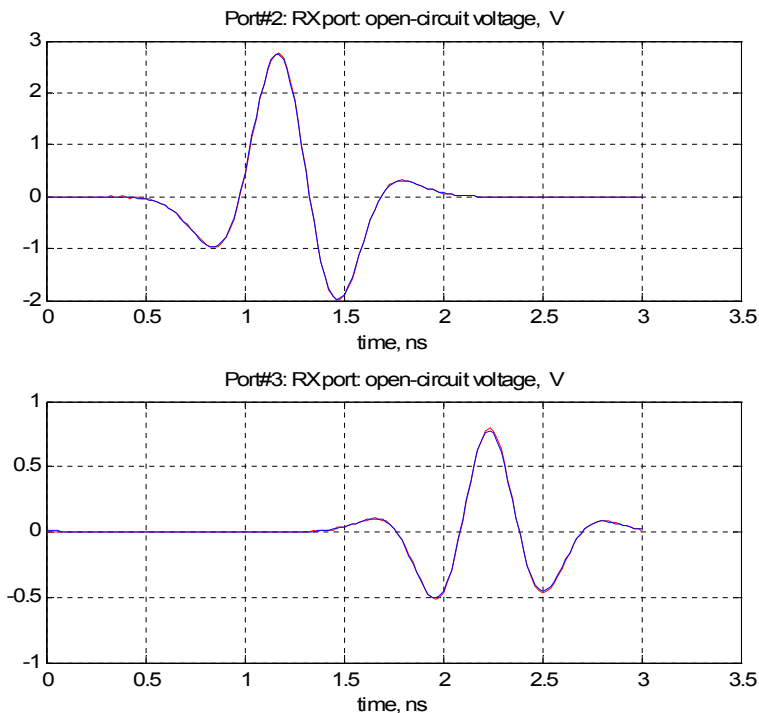


Figure 3-18 Comparison results for a) 20mm and b) 10mm cell size. Blue – exact analytical solution; red – FDTD.

3.4.7 Impressed voltage (electric-field) source in free space

Here, a test case is described for the impressed voltage source, which demonstrates numerical equivalency of the small electric-dipole model (Example 1) and the impressed voltage source. The detail parameters are summarized in Table 3-7

Table 3-7 Test parameters

Domain Size	Cell size	Pulse center frequency/wavelength	Cells per wavelength at center frequency
1.2×1.2×1.2m	20mm or 10mm	800MHz $\lambda = 375\text{mm}$	18.75 or 37.5
Excitation port	Receiver/probe ports		
One voltage source centered at origin and oriented along the z-axis with the moment 10^{-3} m^2 per one volt	Three field probes at the distances 60, 200, and 340mm oriented along the z-axis to sample the radiated vertical electric field in the E-plane (the xz-plane)		

Graphic results can be found below in Fig 3-19. Port #1 indicates the impressed

voltage source, Ports #2~#4 indicate the field probes at the distances 60, 200, and 340mm oriented along the z-axis.

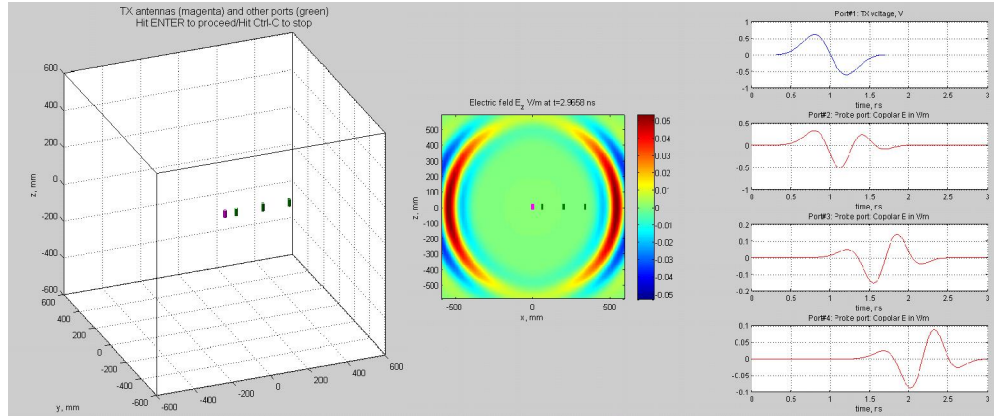


Figure 3-19 a) Test geometry and b) Test output

For harmonic excitation, the vertical E -field component of an infinitesimally-small electric dipole of length l in the xz -plane at $z = 0$ is given in the phasor form [22] by

$$E_z(y, z = 0) = -E_\theta(y, z = 0) = -\eta \left[\frac{1}{r} + jk + \frac{1}{jkr^2} \right] \frac{M_{z0}}{4\pi r} \exp(-jkr) \quad (3-61)$$

where $M_{z0} = Il_0$ is the corresponding dipole moment. Eq. (3-61) can be transformed to the time-domain solution for an arbitrary pulse by operator substitution $jk \rightarrow c_0^{-1} \partial/\partial t$. This yields, in time domain

$$E_z(y, z = 0) = \frac{-\eta}{4\pi r} \left[\frac{M_z(t-r/c_0)}{r} + \frac{1}{c_0} \frac{\partial M_z(t-r/c_0)}{\partial t} + \frac{c_0 \int_0^{t-r/c_0} M_z(t') dt'}{r^2} \right] \quad (3-62)$$

where now

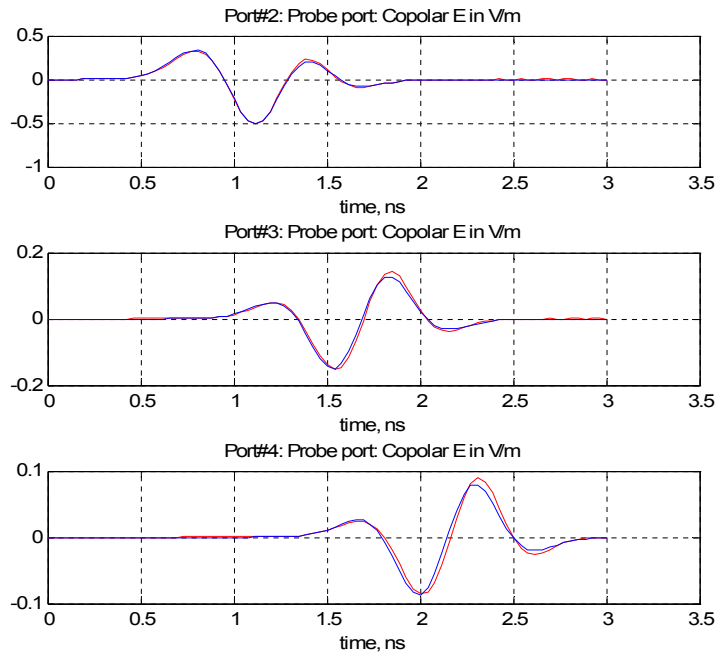
$$M_z(t) = li(t) \quad (3-63)$$

is the instantaneous dipole moment of the small dipole with $i(t)$ being the instantaneous dipole current in amperes. The electric dipole current is to be expressed by $i(t) = Cd v / dt$ where $v(t)$ is the voltage of the impressed voltage

source given by Eq. (3-61) of the introduction and $C = \epsilon_0 A / l$ is the equivalent capacitance. Here, A is the moment of the impressed voltage source (capacitor plate area) with the units of m^2 per one volt.

Fig. 3-20a shows the comparison results between two pulse forms (red-FDTD, blue-analytical) for three probes. The agreement is good for the closest probe, but it becomes slightly worse when the probe is moved from the near field into the Fresnel region. Note that the closest probe is located at the distance of three unit cells (0.16λ) from the antenna.

Fig. 3-20b shows the same results, but when the cell size in this example is reduced to 10mm. All other parameters remain the same. The agreement is now excellent.



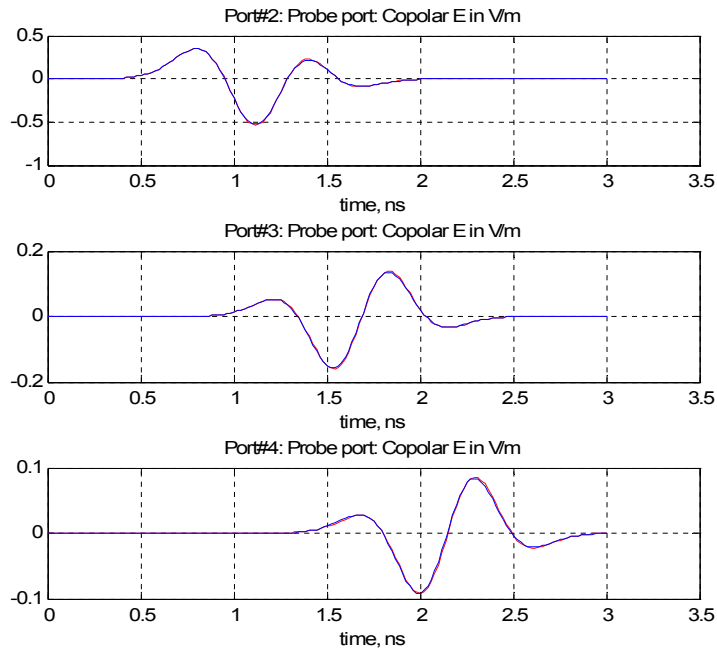


Figure 3-20 Comparison results for a) 20mm and b) 10mm cell size. Blue – exact analytical solution; red – FDTD.

3.4.8 Error Analysis

The relative error, E , is defined as

$$E = \sqrt{\frac{\int_{t_1}^{t_2} (f_{\text{analytical}} - f_{\text{numerical}})^2 dt}{\int_{t_1}^{t_2} (f_{\text{analytical}})^2 dt}} \quad (3-64)$$

Here, the pulse is confined between two time moment: t_1, t_2 .

A summary of the relative errors achieved is given in Table 3-8

Table 3-8 RELATIVE ERRORS COMPARISON BETWEEN STANDARD MODEL AND CPCs MODEL

Test Configuration	Receiver Distance (mm)	20mm Cell Error (%)		10mm Cell Error (5)	
		<i>Standard</i>	<i>CPCs</i>	<i>Standard</i>	<i>CPCs</i>
Elec. Dipole / 3 grid aligned Rx probes	60	33.6	7.4	8.0	0.4
	200	5.7	6.4	1.4	1.6
	340	10.8	11.4	2.6	2.8
Elec. dipole / 4 non-grid aligned probes	60	126.0	7.4	34.7	0.4
	$200\sqrt{2}$	4.9	3.8	1.1	0.8
Mag. Dipole / 3 grid aligned Rx probes	100	2.5	2.5	0.6	0.6
	200	7.7	7.7	1.9	.20
	300	13.5	13.5	3.4	3.4
Mag. Dipole / 2 grid aligned Rx coils	60	6.7	6.7	2.1	2.1
	320	22.8	22.8	5.6	5.6
Mag. Dipole / 2 non-grid aligned Rx probes	$60\sqrt{2}$	16.3	5.4	7.5	1.8
	$260\sqrt{2}$	31.3	8.3	13.9	2.3
Impressed voltage source and three grid aligned Rx probes	60	24.8	6.0	5.9	1.4
	200	10.5	11.1	2.5	2.7
	340	17.5	18.1	4.1	4.3

3.4.9 Analysis of the closest distance

Given these results in previous sections, the question arises as to how close infinitesimal CPCs source and receiver elements can be placed to each other. The progression from one to three cells of separation distance is quantified in Table 3-9 and depicted from left to right in Fig. 3-21.

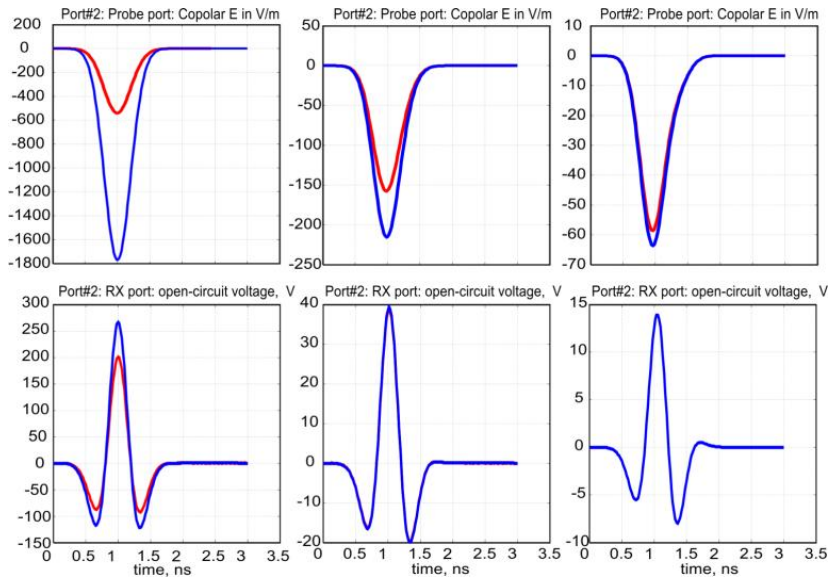


Figure 3-21 Copolar fields close to the dipole (top) and coil (bottom) as spacing moves from one cell (left) to three (right).

Based on these results, a minimum separation distance of three cells is required in order to obtain reasonable (i.e., error < 10%) results. A magnetic dipole seems perform better than the electric dipole and can still achieve relative good (~20%) results even in the case of one cell separation case and the error reduce quickly when the distance increase to 2 cells.

Table 3-9 EXAMINATION OF SOURCE SEPARATION

Case	Separation Distance (cells)	Error (%)	
		19 cells/ λ	38 cells/ λ
Electric Dipole	1	70.3	69.0
	2	27.4	26.2
	3	7.4	7.8
Magnetic Dipole	1	21.2	25.2
	2	2.2	1.8
	3	5.4	1.4

CHAPTER 4

CONCLUSIONS

We conclude that the CPCs model performs either equally well or better than the standard model for grid and non-grid aligned problems, respectively. For non-grid aligned problems, the error is reduced by the factor of four or more in the near field (at distances about 0.16λ from the source). A minimum separation distance of three cells is required in order to obtain integral error less than 10% for the coincident phase-center electric dipole sources. Magnetic dipole sources can achieve a better result with the error remaining less than 10% in the two-cells distance.

To take advantage of the property of the CPCs coil sources, two small orthogonal coils has been considered to create a highly-directional single-lobe beam [4].

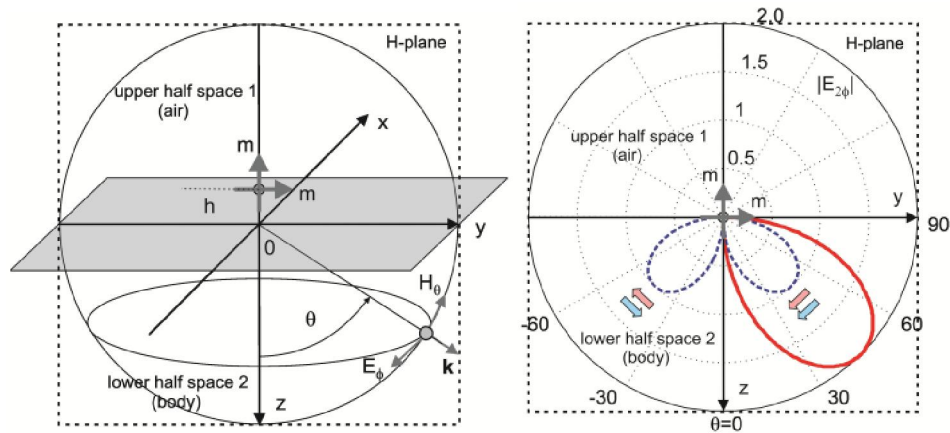


Figure 4-1 Geometry and H-plane definition (left) and normalized patterns into the lower half-space (right)

The highly-directional antenna can be applied to inside human body localization purpose and a variety other kinds of application in localization and WBAN.

BIBLIOGRAPHY

- [1] K.S.Yee, "Numerical solution of initial boundary value problem involving Maxwell's equations in isotropic media," *IEEE Trans. Antennas and Propagation*, vol. 14, pp. 302-307, 1966.
- [2] A.Taflove, Computational Electrodynamics, The Finite Difference Time Domain Approach, 3rd ed., MA: Artech House, 2005.
- [3] G. M. Noetsche, S. M. Makarov and N. Clow, "Modeling accuracy and features of body-area networks with out-of-body Antennas at 402 MHz," *IEEE Antennas and Propagation Magazine*, vol. 53, no. 4, pp. 118-143, 2011.
- [4] G. M. Noetscher and S. N. Makarov, "Directional in-quadrature orthogonal-coil antenna and an array thereof for localization within a human body in a Fresnel region," in *IEEE AP-S/USNC-URSI Int. Sym.*, Chicago, 2012.
- [5] R. Holland, "Finite-difference time-domain (FDTD) analysis of magnetic diffusion," *IEEE Trans. Electromagnetic Compatibility*, vol. 36, pp. 32-39, 1994.
- [6] G. Marrocco, M. sabbadini and F. Bartadi, "FDTD Improvement by Dielectric Subgrid Resolution," *IEEE Trans. Microwave Theory Techniques*, vol. 46, no. 12, pp. 2166-2169, 1998.
- [7] K. S. Kunz and R. Luebbers, [K. S. Kunz and R. Luebbers, The Finite Difference Time Domain Method, Boca Raton, FL: CRC Press, 1993.
- [8] G. Mur, "Absorbing boundary conditions for the finite-difference approximation of the time-domain electromagnetic field equations," *IEEE Trans. Electromagnetic Compatibility*, Vols. EMC-23, no. 4, pp. 377-382, 1981.
- [9] K. K. Mei and J. Fang, "Superabsorption – a method to improve absorbing boundary conditions," *IEEE Trans. Antennas and Propagation*, vol. 40, no. 9, pp. 1001-1010, 1992.
- [10] N. V. Kantartzis and T. D. Tsiboukis, "A comparative study of the Berenger perfectly matched layer, the superabsorption technique, and several higher-order ABCs for the FDTD algorithm in two and three dimensional problems," *IEEE Trans. Magnetics*, vol. 33, no. 2, pp. 1460-1463, 1997.
- [11] J.-P. Bérenger, "A perfectly matched layer for the absorption of electromagnetic waves," *J.Comput. Phys*, vol. 114, pp. 185-200, Oct 1994.
- [12] D. S. Katz, E. T. Thiele and A. Taflove, "Validation and extension to three dimensions of the Berenger PML absorbing boundary condition for FD-TD meshes," *IEEE Microwave and Guided Wave Letters*, vol. 4, no. 8, pp. 268-270, Aug 1994.
- [13] C. E. Reuter, R. M. Joseph, E. T. Thiele, S. Katz and A. Taflove, "Ultrawideband absorbing boundary condition for termination of waveguiding structures in FD-TD simulations," *IEEE Microwave and Guided Wave Letters*, vol. 4, no. 10, pp. 268-270, oct 1994.
- [14] Z. S. Sacks, D. M. Kingsland, R. Lee and J.-F. Lee, "A perfectly anisotropic absorber for use as an absorbing boundary condition," *IEEE Trans. Antennas and Propagation*, vol. 43, pp. 1460-1463, Dec 1995.
- [15] J.-P. Bérenger, "Numerical reflection from FDTD-PMLs: a comparison of the split PML with the unsplit and CFS PMLs," *IEEE Trans. Antennas and Propagation*, vol. 50, pp. 258-265,

2002.

- [16] S. D. Gedney, "An anisotropic perfectly matched layer-absorbing medium for the truncation of FDTD lattices," *IEEE Trans. Antennas and Propagation*, vol. 44, pp. 1630-1639, Dec 1996.
- [17] J.-P. Bérenger, "Three-dimension perfectly matched layer for the absorption of electromagnetic waves," *J.Comput. Phys*, vol. 127, pp. 363-379, 1996.
- [18] J.-P. Bérenger, "Perfectly matched layer for the FDTD solution of wavestructure interaction problems," *IEEE Trans. Antennas and Propagation*, pp. 110-117, Jan 1996.
- [19] R. Pontalti, J. Nadobny, P. Wust, A. Vaccari and D. Sullivan, "Investigation of Static and Quasi-Static Fields Inherent to the Pulsed FDTD Method," *IEEE Trans. Microwave Theory Techniques*, vol. 50, no. 8, pp. 2022-2025, 2002.
- [20] G. S. Smith, "Loop Antennas," in *Antenna Engineering Handbook*, 4th ed., McGraw Hill, 2007, pp. 5-3.
- [21] B. Z. Kaplan and U. Suissa, "Evaluation of inductance for various distributions of windings on straight ferromagnetic cores: an unusual approach," *IEEE Trans. Magnetics*, vol. 38, no. 1, pp. 246-249, 2002.
- [22] C. A. Balanis, *Antenna Theory: Analysis and Design*, 3rd ed., New York: Wiley, 2005.
- [23] S. N. Makarov, "Theory and Manual," [Online]. Available: <https://www.nevaelectromagnetics.com/solver.html>.
- [24] S. N. Makarov, "Validation Examples," [Online]. Available: <https://www.nevaelectromagnetics.com/solver.html>.
- [25] G. M. Noetscher, Y. Xu and S. N. Makarov, "Accuracy of point source models with coincident phase centers in a cubic FDTD grid for arbitrary source orientation," in *IEEE AP-S/USNC-URSI Int. Sym.*, Chicago, 2012.
- [26] A. Elsherbeni and V. Demir, *The Finite-Difference Time-Domain Method for Electromagnetics with MATLAB Simulations*, Raleigh, NC: SciTech Publishing, 2009.
- [27] C. A. Balanis, *Advanced Engineering Electromagnetics*, New York: Wiley, 1989.
- [28] G. M. Noetscher, Y. Xu and S. N. Makarov, "Body area antenna link modeling using MATLAB® engine," in *35th Antenna Applications Symposium*, Monticello, 2011.
- [29] F. T. Ulaby, E. Michielssen and U. Ravaiol, *Fundamentals of Applied Electromagnetics*, 6th ed., Prentice Hall, 2010.
- [30] J.-P. Bérenger, "Evanescent waves in PML's: Origin of the numerical reflection in wave-structure interaction problems," *IEEE Trans. Antennas and Propagation*, vol. 47, pp. 1497-1503, Oct 1999.
- [31] J.-P. Bérenger, "On the Huygens absorbing boundary conditions for electromagnetics," *J.Comput. Phys*, vol. 226, pp. 354-378, 2007.
- [32] J.-P. Bérenger, *Perfectly Matched Layer (PML) for Computational Electromagnetics*, Morgan & Claypool, 2007.